



Crustal conductivity and distribution of melt beneath the Krafla caldera, N-Iceland inferred from magnetotelluric data

Rifqa Agung Wicaksono



**Faculty of Earth Sciences
University of Iceland
2010**

Crustal conductivity and distribution of melt beneath the Krafla caldera, N-Iceland inferred from magnetotelluric data

Rifqa Agung Wicaksono

60 ECTS thesis submitted in partial fulfillment of a
Magister Scientiarum degree in Sustainable Energy

Supervisors

Gylfi Páll Hersir
Bryndís Brandsdóttir

Examiner

Knútur Árnason

Faculty of Earth Sciences
School of Engineering and Natural Sciences
University of Iceland
Reykjavik, January 2010

Crustal conductivity and distribution of melt beneath the Krafla caldera, N-Iceland inferred from magnetotelluric data

Crustal conductivity and distribution of melt

60 ECTS thesis submitted in partial fulfillment of a *Magister Scientiarum* degree in Sustainable Energy

Copyright © 2010 Rifqa Agung Wicaksono
All rights reserved

Faculty of Earth Sciences
School of Engineering and Natural Sciences
University of Iceland
Sturlugata 7,
101 Reykjavík
Iceland

Telephone: 525 4600

Bibliographic information:

Wicaksono, R. A., 2010, *Crustal conductivity and distribution of melt beneath the Krafla caldera, N-Iceland inferred from magnetotelluric data*, Master's thesis, Faculty of Earth Sciences, University of Iceland, 77 pp.

Printed by Háskólaprent ehf.
Reykjavik, Iceland, January 2010

Abstract

Subsurface resistivity structure across the divergent plate boundary of Iceland is characterized by thin, intermittent near-surface high conductivity layers associated with geothermal alteration and a thick, mid-crustal conductor deepening away from the plate boundary. In addition, one-dimensional magnetotelluric (MT) models of the Krafla central volcano have revealed two anomalous, updoming zones of high conductivity beneath the Krafla caldera overlapping partly shear wave shadow zones interpreted as areas of melt accumulation during the 1974-1989 rifting episode. To further constrain the extent of the updoming conductors and elucidate their relationship with the lower crustal conductor as well as near surface anomalies two-dimensional magnetotelluric inversions were conducted along two east-west profiles across the Krafla caldera. The northern profile which crosses both shear-wave shadow zones reveals a single updoming conductor within the western zone suggesting that the northern boundary of the eastern zone is located just south of the profile. Sensitivity tests indicate that the dimensions of the updoming conductor (0.5 – 2 km wide and 4 – 5 km high) are in a good agreement with seismic and geodetic data. The conductive dome connects with a near-surface conductive layer, at less than 500 m, which correlates with surface geothermal manifestations and the mid crustal connector, at 6-16 km depth. The top of the deeper conductor correlates fairly well with the brittle-ductile crustal boundary. Although joint interpretation of magnetotelluric data with other geophysical data further illuminates the geometrics of the shallow magma system of Krafla the percentage of partial melt within the mid-crustal conductor remains unknown.

I would like to dedicate my thesis to my beloved parents, sister and brothers.

Table of Contents

List of Figures	viii
Symbols and variables.....	x
Acknowledgements	xi
1 Introduction.....	1
2 Geological overview of the study area.....	5
3 Magnetotelluric (MT) method	7
3.1 Basic theory	7
3.2 Field measurement	13
3.3 From time series to frequency domain	14
4 MT data	19
4.1 MT apparent resistivity and phase.....	19
4.2 Dimensionality and strike direction	23
4.3 Static shift correction.....	26
5 1-D MT data inversion	29
5.1 The 1-D MT inversion.....	29
5.2 TEM-MT joint 1-D inversion.....	29
5.3 1-D resistivity model of Krafla	30
6 2-D MT data inversion	35
6.1 The 2-D MT inversion.....	35
6.2 2-D resistivity model of Krafla	36
7 Analysis and discussions.....	45
7.1 Structure of the upper 3 km	45
7.2 Midcrustal and deeper structures.....	48
7.3 Sensitivity test	52
8 Conclusions.....	55
References	57
Appendix A: From Maxwell's equations to the diffusion equations	61
Appendix B: Observed data and calculated responses from TMTE joint inversion.....	63

List of Figures

Figure 1. A tectonic map of the Northern Volcanic Zone.....	2
Figure 2. Aerial image of the Krafla caldera and surrounding region.....	6
Figure 3. Simple half-space uniform earth model	9
Figure 4. Simple 1-D layered earth model.	11
Figure 5. Simple 2-D model and the concept of polarization in magnetotellurics.....	12
Figure 6. Transverse magnetic (TM) and transverse electric (TE) mode in magnetotellurics.....	13
Figure 7. Field layout of a 5-channel MT data acquisition system.	14
Figure 8. An example of magnetotelluric processing results.	16
Figure 9. Location of the MT soundings and profiles.	19
Figure 10. An example of resampled MT data.....	20
Figure 11. Apparent resistivity and phase pseudo-sections along the MT profile in TM and TE mode.....	21
Figure 12. Swift's skew for all sites at different periods	25
Figure 13. Preferred Zstrike direction of each MT site at different periods.	27
Figure 14. TEM sounding setup.	28
Figure 15. An example of 1-D TEM/MT joint inversion.....	30
Figure 16. 1-D resistivity cross sections of MT soundings on profile AV7290.....	32
Figure 17. 1-D resistivity cross sections of MT soundings on profile AV7288.....	33
Figure 18. 1-D resistivity cross sections of MT soundings on profile KRF-2	34
Figure 19. An example of a mesh grid design.....	36
Figure 20. The 2-D inversion (REBOCC) models for AV7290.....	38
Figure 21. The 2-D inversion (REBOCC) model for AV7288	40
Figure 22. Measured and calculated apparent resistivity and impedance phase pseudo-section from the model of the AV7290 profile.....	42
Figure 23. Measured and calculated apparent resistivity and impedance phase pseudo-section from the model of the AV7288 profile.....	43

Figure 24. Comparing 1-D and 2-D results of profile AV7290.	46
Figure 25. Comparing 1-D and 2-D results of profile AV7288.	47
Figure 26. Simplified representation of thermal environment of the active magma chamber..	48
Figure 27. De-trended Bouguer gravity map of Krafla..	49
Figure 28. A map showing the depth to the deeper conductor in the Icelandic crust and a 1-D MT profile crossing the Krafla volcanic system.....	50
Figure 29. TM mode of AV7290 compared to the pervious study	51
Figure 30. Apparent resistivity and impedance phase sounding curves of the TM mode at site K-81494 in the western part of profile AV7290.	53

Symbols and variables

A_r	effective area of the Transient Electro-Magnetic receiver coil [m^2]
A_s	effective area of the Transient Electro-Magnetic source loop [m^2]
\mathbf{B}	magnetic field [Tesla (T) = V s m^{-2}]
\mathbf{D}	electric displacement [$\text{C m}^{-2} = \text{A s m}^{-2}$]
\mathbf{E}	electric field [V m^{-1}]
E_x, E_y	horizontal components of \mathbf{E} in Cartesian co-ordinates [V m^{-1}]
f	frequency [Hz]
\mathbf{H}	magnetic field intensity [A m^{-1}]
H_x, H_y, H_z	three components of \mathbf{H} in Cartesian co-ordinates [A m^{-1}]
I	current [A]
\mathbf{J}	electric current density [A m^{-2}]
k	wave number [m^{-1}]
S_{xy}, S_{yx}	static shift multipliers of TE and TM mode
t	time [s]
T	period [s]
V	voltage [V]
x, y, z	Cartesian co-ordinates (z positive downward)
\mathbf{Z}	impedance tensor [V A^{-1}]
$Z_{xx}, Z_{xy}, Z_{yx}, Z_{yy}$	elements of \mathbf{Z} [V A^{-1}]
α	rotational angle [$^\circ$]
δ	skin depth [m]
ϵ	electric permittivity [$\text{A s V}^{-1} \text{m}^{-1} = \text{F m}^{-1}$]
μ, μ_0	magnetic permeability, magnetic permeability of free space [$\text{V s A}^{-1} \text{m}^{-1} = \text{H m}^{-1}$]
ρ	resistivity [$\Omega\text{m} = \text{V m A}^{-1}$]
ρ_a	apparent resistivity [$\Omega\text{m} = \text{V m A}^{-1}$]
σ	conductivity [$\text{S m}^{-1} = \text{A V}^{-1} \text{m}^{-1}$]
ϕ	phase [$^\circ$]
ω	angular frequency [s^{-1}]

Acknowledgements

In the first place I would like to record my gratitude to Gylfi Páll Hersir and Bryndís Brandsdóttir for their supervision, advice, and guidance from the very early stage of this research as well as giving me extraordinary experiences throughout the work. Above all and the most needed, they provided me unflinching encouragement and support in various ways. I also benefited by outstanding works from Knútur Árnason, Hjálmar Eysteinnsson, Arnar and Guðni and all the people in ÍSOR.

I wish to thank Reykjavik Energy Graduate School of Sustainable Systems (REYST) through Edda Lilja Sveinsdóttir for offering an MSc scholarship for me. This scholarship made it possible for me to travel to Iceland to conduct my study. I would also like to thank Landsvirkjun through Ásgrímur Guðmundsson for supplying MT and TEM data and for giving permission to publish these results.

Many thanks go in particular to all MSc fellows in the United Nation University Geothermal Training Program: Hari Koestono for his great support and hospitality, Yohannes Lemma Didana for all great discussions around geophysical methods, Manuel Rivera, Kiflom Gebrehiwot and Erlindo Angcoy for their support and discussion.

My special thanks go to Indra Budi Suryata, without him; this thesis would be unintelligible to read at all due to my “poor” English.

No one, however, help me more directly and continuously in writing this thesis than my beloved family in Indonesia. Without their love, this thesis could not have been written.

Lastly, I offer my regards and blessing to all of those who supported me in any respect during the completion of the project.

1 Introduction

The divergent plate boundary of Iceland is made up of numerous volcanic systems, forming an echelon segments along the rift zones (Figure 1). The Krafla volcanic system in N-Iceland is one of the best-studied volcanic system, being the center of a rifting episode in 1974-1989 which activated an approximately 100 km long segment of the divergent plate boundary. This magmatic and tectonic episode was characterized by inflation/deflation cycles which were controlled by increasing/decreasing magma pressure within a shallow crustal magma chamber beneath the Krafla caldera and tectonic stress at the plate boundary (Björnsson et al., 1977; Björnsson, 1985; Einarsson, 1978, Tryggvason, 1999; Buck et al., 2006). Magma accumulated within a shallow magma chamber beneath the caldera region during inflation periods and was intruded into the transecting fissure swarm or extruded in basaltic fissure eruptions during brief deflation events. The recent magmatic activity replenished the Krafla magma chamber and active geothermal areas within the caldera.

Although the Krafla rifting episode provided valuable information on magmatic and tectonic processes within a divergent volcanic system the geometry of the shallow Krafla magma chamber (Einarsson, 1978) and possible deeper reservoirs (Tryggvason, 1986; Árnadóttir et al., 1998) has remained poorly constrained. Using local microearthquakes recorded by analog one-component instruments, Einarsson (1978) mapped two shear-wave shadow zones within the Krafla caldera as representing magma accumulation below a depth of 3 km. The shear wave shadow zones are elongated EW with an unclear lower boundary. The eastern zone encompasses the Krafla geothermal field presently utilized by the Krafla geothermal power plant, whereas the western zone is located west of the Leirhnjúkur geothermal field. The northern boundary of the western zone is poorly constrained (Einarsson, 1978). In order to further constrain the dimensions of the Krafla magma chamber, Brandsdóttir and Menke (1992) performed waveform studies on earthquakes which originated in the Krafla caldera during a brief inflation period in July 1988. They identified reflections from the base of the magma chamber which indicated its thickness to be less than 1 km in the central northern part of the caldera. However, they were unable to constrain its lateral dimensions. Refraction modeling further constrained the thickness of the Krafla magma chamber as being less than 2 km and illuminated its seating on top of a broad high-velocity dome extending from the lower crust (11-14 km depth) beneath the central volcano (Brandsdóttir et al., 1997). Furthermore, shear waves, reflected from a 19 km deep Moho indicated that the midcrust beneath the magma chamber cannot contain high percentage of partial melt or even be at near-solidus temperatures.

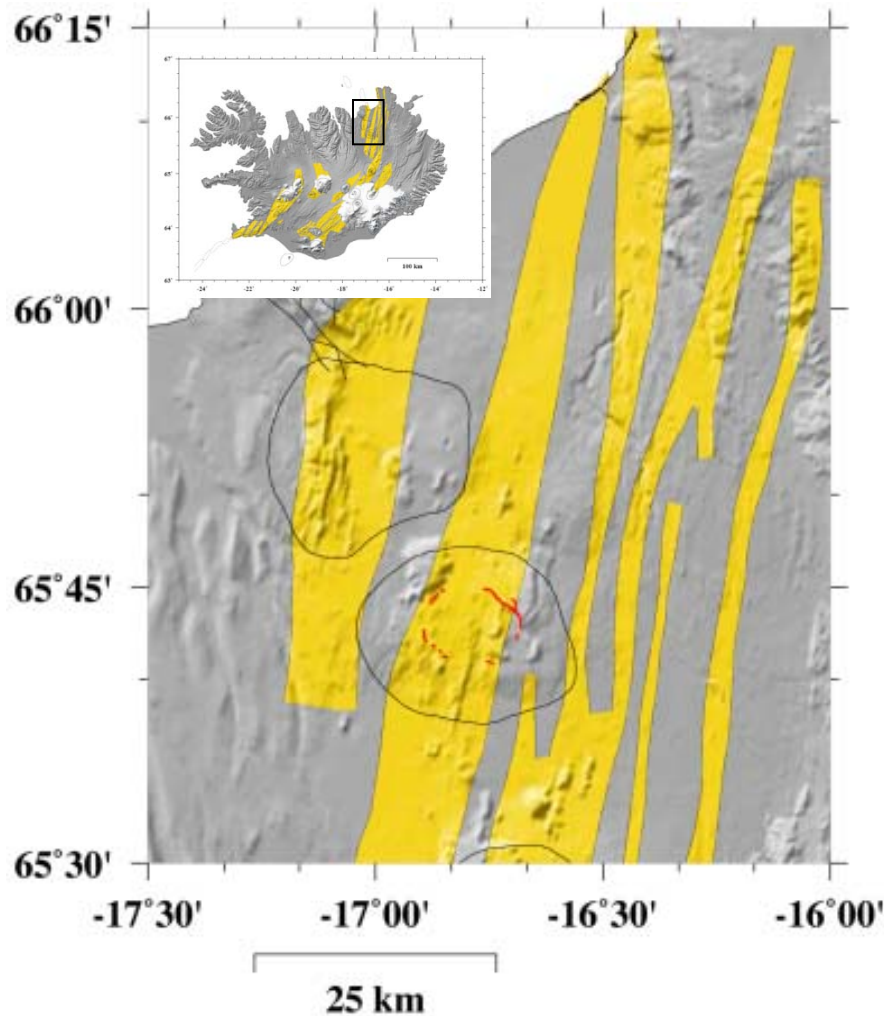


Figure 1. A tectonic map of the Northern Volcanic Zone based on a map (inset) by Einarsson and Sæmundsson (1987). The fissure swarms (yellow regions) transect the central volcanoes of the volcanic systems (black lines). The Krafla caldera is denoted by the red lines.

Geodetic measurements support the existence of a shallow magma chamber at a depth of 2-3 km within the caldera and have been used to argue for the existence of multiple magma reservoirs at depth (Tryggvason, 1986; Árnadóttir et al., 1998; de Zeeuw-van Dalfsen et al., 2004). The mean center of inflation during 1975-1989 was determined by tilt and distance measurements to lie at 2 and 3 km depth near 65°N 42,883' and -16°W 47.983', about 500 m southwest of Leirhnjúkur (Tryggvason, 1999). Several shallow source subsidence centers in vicinity of Leirhnjúkur, determined by Interferometric Synthetic Aperture Radar (InSAR) images in 1992-1999 have been interpreted as due to cooling and contraction of the Krafla magma chamber whereas uplift over a 50 km wide area has been attributed to magma accumulation near the crust-mantle boundary rather than post-rifting adjustment (Sigmundsson et al., 1997; de Zeeuw-van Dalfsen et al., 2004, Sturkell et al., 2008). Levelling surveys, InSAR images and repeated gravity surveys show the area of deflation to be of limited extent, spanning an area with a radius less than 2 km, within the center of the caldera, between the two shear wave attenuation zones (Sigmundsson et al., 1997; de Zeeuw-van Dalfsen et al., 2004, 2006; Sturkell et al., 2008).

One-dimensional (1-D) interpretation of magnetotelluric (MT) measurements to investigate vertical and lateral variations of the electrical resistivity in the lower crust and upper mantle within the Northern Volcanic Zone was initiated by Beblo and Björnsson (1978, 1980) and Beblo et al. (1983). They revealed the evidence of a low-resistivity layer deepening away from the Krafla Central Volcano. Subsequent MT campaigns within the Krafla region focused on subsurface resistivity structure within the upper crust in association with geothermal exploration within the Krafla caldera (Árnason et al., 2009; Mortensen et al., 2009). Using 1-D models of TEM/MT data correlated with gravity and seismic data Árnason et al. (2009) delineated updoming low resistivity bodies below 2.5 km depth beneath Leirhnjúkur and Mt. Krafla overlapping partly the shear wave shadow zones mapped by Einarsson (1978). A third low resistivity anomaly is observed near Sata, within the fissure swarm in the southwest caldera region. The Leirhnjúkur low resistivity dome lies north of the inflation/deflation centers, overlapping the eastern half of the western shear wave shadow zone.

The aim of this study is to jointly interpret 2-D MT inversion of MT data and available seismic and gravity data in order to constrain the dimensions of shallow magma reservoirs beneath the Krafla caldera and elucidate their relationship with the lower crustal conductors as well as near surface high-temperature geothermal areas.

2 Geological overview of the study area

Iceland is situated on top of a hotspot associated with a mantle plume coinciding with the mid-Atlantic ridge. This interaction has generated segmented plate boundary with volcanic zones composed of numerous volcanic systems (Einarsson, 2008) and thick oceanic crust. Each volcanic system consist of a central volcano and transecting fissure swarm which represents the spreading segment. The central volcano where the major eruptive activity is commonly circular in outline and 20 to 40 km in diameter, whilst its transecting fissure swarm is usually between 10 to 100 km long and 20 km wide. Most of the high-temperature geothermal systems are associated with these volcanic systems.

The Northern Volcanic Zone (NVZ) is composed of seven NNE-SSW elongated volcanic systems arranged en echelon along the plate boundary, including Krafla (Figure 1). Fissure swarms, characterized by rifting structures such as crater rows, normal faults, and open fissures transect the central volcanoes at an azimuth perpendicular to the regional spreading direction (Sæmundsson, 1978; Einarsson and Sæmundsson, 1987). The Krafla volcanic system is characterized by an approximately 20 km wide central volcano, engulfing a 10 km wide (EW) and 7-8 km long (NS) caldera. The central volcano is made up of alternating basaltic lava and hyaloclastite sequences with gently sloping topographic highs ranging from 300 to 500 m in elevation whereas individual hyaloclastite table mountains and rhyolitic ridges reach 900 m elevation. (Figure 2). The Krafla caldera, formed during the last interglacial period, about 100,000 years ago, has since been filled with eruptive products. The caldera has thus been defined based on geological mapping of cone dikes and semi-acidic welded tuff produced at the caldera formation (Sæmundsson, 1991). The Krafla central volcano is transected by a NNE-SSW trending fissure swarm, extending from the Mývatn region about 100 km northwards to Axarfjörður (Sæmundsson, 1991).

Two high-temperature geothermal areas can be founded within the Krafla volcanic system. One within the caldera (the Krafla-Leirhnjúkur geothermal field) and south of the caldera (the Bjarnarflag-Námafjall field). The Krafla geothermal power plant utilizes the eastern part of the Krafla-Leirhnjúkur geothermal field.

At least twenty inflation/deflation cycles occurred during the Krafla rifting episode. During inflation periods, intense seismicity was observed in the crust above the magma chamber due to increasing pressure in the Krafla magma chamber while seismicity along the fissure swarm characterized deflation events (Buck et al., 2006). Mapping shear wave attenuation, Einarsson (1978) delineated two regions within the caldera suggested to contain melt. The overall region is 2-3 km width in N-S direction and 8-10 km in the E-W direction (Figure 2). Recent compilation of old and newer geophysical data indicates that an inner caldera may exist (Árnason et al., 2009).

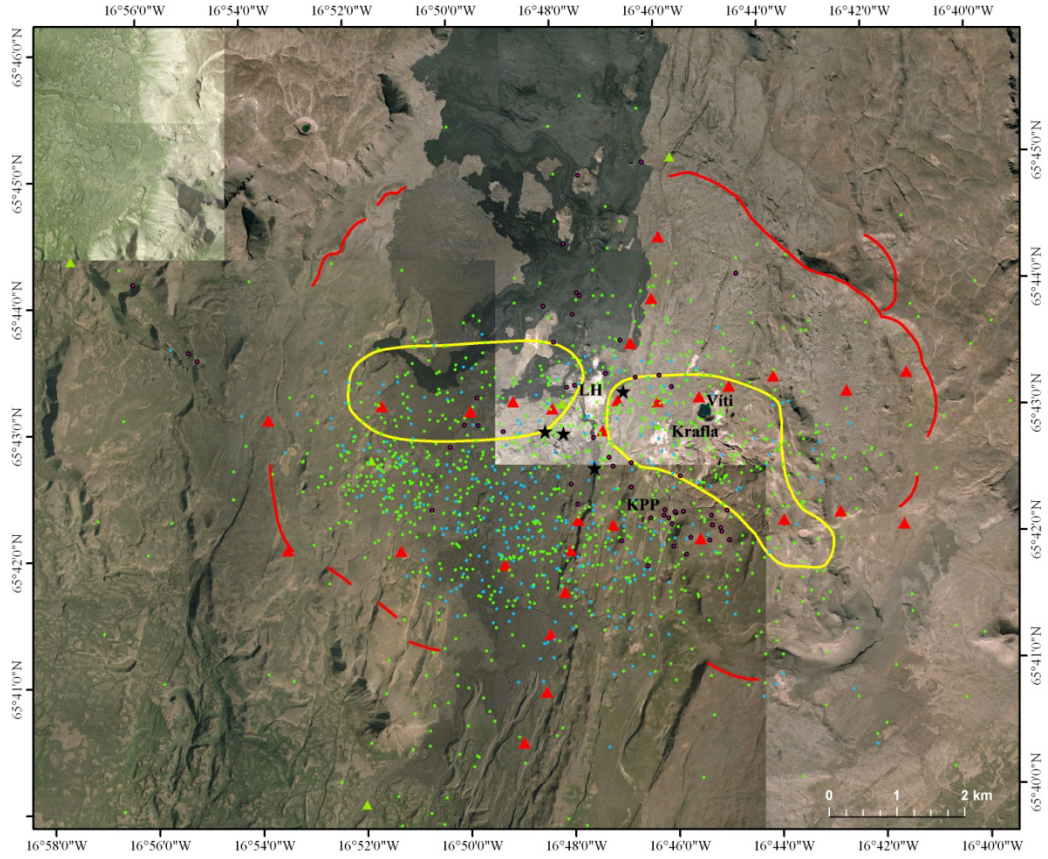


Figure 2. Aerial image of the Krafla caldera and surrounding region showing MT survey sites (red triangle) within the Krafla caldera (marked by red lines), shear wave shadow zones (yellow lines) delineated by Einarsson (1978), earthquake epicenters during the inflation periods 1974-1980 (green dots) and 1988 (blue dots) located by the IMO network. Black stars denote inflation and deflation centers determined by geodetic and InSAR surveys (Sigmundsson et al., 1997; Tryggvason, 1999; de Zeeuw-van Dalfsen et al., 2004; Sturkell et al., 2008). The location of Leirhnjúkur is marked by LH and Krafla Power Plant by KPP.

3 Magnetotelluric (MT) method

3.1 Basic theory

Magnetotellurics (MT) is a passive geophysical method which involves the comparison of the fluctuating horizontal components of the magnetic and electric fields on the earth's surface (Tikhonov, 1950; Cagniard, 1953). Two known sources of electromagnetic field are harnessed by this method: a.) The magnetic field which is produced by the interaction between solar winds and the Earth's magnetosphere and causes electromagnetic fluctuations that induce currents in the earth (frequencies lower than 1 Hz); and b.) The electromagnetic field originated by the meteorological activity such as lightning discharges (frequencies higher than 1 Hz). The MT method exploits the electromagnetic field with periods ranging from $\sim 10^{-3}$ to $\sim 10^5$ s.

The basic theory of the MT method is based on Maxwell's equations which describe the behavior of the electromagnetic field. These equations are expressed as:

$$\nabla \times \mathbf{E} = -\frac{\partial \mathbf{B}}{\partial t}, \quad (3.1a)$$

$$\nabla \times \mathbf{H} = \mathbf{J} + \frac{\partial \mathbf{D}}{\partial t}, \quad (3.1b)$$

$$\nabla \cdot \mathbf{B} = 0, \quad (3.1c)$$

$$\nabla \cdot \mathbf{D} = \eta_f, \quad (3.1d)$$

where \mathbf{H} is the magnetic intensity (A/m), \mathbf{J} is the electric current density (A/m^2), \mathbf{D} is the electric displacement (C/m^2), \mathbf{E} is the electric field intensity (V/m), \mathbf{B} is the magnetic induction (T), and η_f is the electric charge density (C/m^3).

These four equations together with the constitutive relations for a homogeneous linear isotropic medium are used to derive the diffusion equations in terms of the time-varying electric and magnetic field (see Appendix A):

$$\nabla^2 \mathbf{E} = \nabla \times \frac{\partial \mathbf{B}}{\partial t} = \mu \frac{\partial}{\partial t} (\nabla \times \mathbf{H}) = \mu \sigma \frac{\partial \mathbf{E}}{\partial t} + \epsilon \mu \frac{\partial^2 \mathbf{E}}{\partial t^2} \quad (3.2a)$$

$$\nabla^2 \mathbf{B} = -\sigma (\nabla \times \mathbf{E}) - \epsilon \frac{\partial}{\partial t} (\nabla \times \mathbf{E}) = \mu \sigma \frac{\partial \mathbf{B}}{\partial t} + \epsilon \mu \frac{\partial^2 \mathbf{B}}{\partial t^2} \quad (3.2b)$$

Both equations represent the behavior of the electromagnetic field propagations in two different ways: a diffusive ($\mu \sigma \frac{\partial \mathbf{E}}{\partial t}$ and $\mu \sigma \frac{\partial \mathbf{B}}{\partial t}$) and a non-diffusive wave propagation ($\epsilon \mu \frac{\partial^2 \mathbf{E}}{\partial t^2}$ and $\epsilon \mu \frac{\partial^2 \mathbf{B}}{\partial t^2}$). Both of them are frequency dependent.

In MT studies, the variations in electric permittivities, ϵ , and magnetic permeabilities, μ , of rocks are negligible compared with variations in bulk conductivities. Therefore free-space values ($\epsilon_0 = 8.85 \times 10^{-12}$ F/m and $\mu_0 = 1.2566 \times 10^{-6}$ H/m) are assumed. One of the assumption in magnetotellurics is the quasistatic approximation, which states that the electrical conduction currents are always much larger than the electrical displacement current (the earth is such a good conductor, that is $\sigma \gg \omega \epsilon$). Therefore,

eq. 3.2a and 3.2b are reduced to only first partial time derivatives form and define the fields that are diffused downward into the earth.

Another assumption in magnetotellurics is that the plane wave is assumed to be normally incident. This is certainly not true for waves from all sources which are superimposed and form the resultant at a given measurement site at a given time. But all waves, irrespective of their incoming directions are refracted almost vertically (normally) into the earth. This can be explained by the Snell's law, consider the plain electromagnetic wave of angular frequency ω and wave vector \mathbf{k}_0 incident at the surface of a homogeneous earth with resistivity $\rho = l/\sigma$. The wave vector \mathbf{k}_0 makes the angle θ_i (angle of incident) with the z-axis. A refracted wave propagates into the half-space with wave vector \mathbf{k} making the angle θ_t with the z-axis. Therefore, we have

$$\frac{1}{v_0} \sin \theta_i = \frac{1}{v} \sin \theta_t \quad (3.3)$$

where v_0 and v are the velocities in the air and the half-space (from eq. 3.9), respectively:

$$v_0 = \frac{1}{\sqrt{\epsilon\mu}}; \quad v = \sqrt{\frac{2\omega}{\mu\sigma}} \quad (3.4)$$

then we have

$$\sin \theta_t = \sin \theta_i \sqrt{\frac{2\epsilon\omega}{\sigma}} \quad (3.5)$$

Assuming that the resistivity of ground rocks has range of $1-10^4 \Omega\text{m}$ (therefore, $\rho = l/\sigma < 10^4 \Omega\text{m}$) and the frequency used in MT is less than 10^3 Hz ($\omega < 10^3 \text{ Hz}$), then

$$\frac{2\epsilon\omega}{\sigma} < 10^{-7}$$

So that θ_t is practically zero and refracted wave in the earth has the wave vector \mathbf{k} along the z-axis for all angles of incidence.

For the homogeneous half-space earth (Figure 3), with conductivity σ and a normally incident plane wave, the \mathbf{E} and \mathbf{H} fields are constant in direction and magnitude over planes perpendicular to the vertical, downward +z, direction of propagation. If the field vary harmonically in time, that is as $e^{i\omega t}$ we get:

$$\nabla^2 \mathbf{E} + k^2 \mathbf{E} = 0; \quad \nabla^2 \mathbf{H} + k^2 \mathbf{H} = 0 \quad (3.6)$$

where k is the wave number

$$k = \sqrt{-i\mu\sigma\omega} \quad (3.7)$$

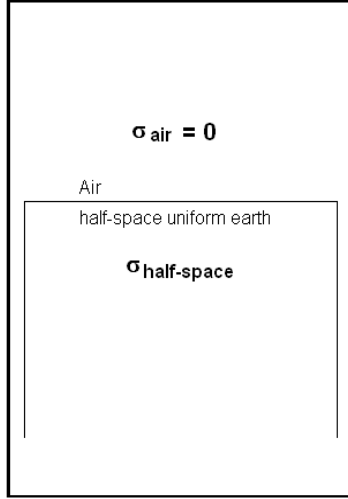


Figure 3. Simple half-space uniform earth model (after Simpson and Bahr, 2005)

For a wave propagating in the direction of \mathbf{u} with the wave vector $\mathbf{k} = k\mathbf{u}$, Maxwell's equation 3.1b shows that

$$-i\mathbf{k} \times \mathbf{H} = \sigma \mathbf{E} = \frac{ik^2}{\mu\omega} \mathbf{E} \quad (3.8)$$

and for the wave propagating along z-axis ($\mathbf{u} = (0,0,1)$ and $\mathbf{u} \times \mathbf{H} = (-H_y, H_x, 0)$), we have:

$$E_x = \frac{\mu\omega}{k} H_y; \quad E_y = -\frac{\mu\omega}{k} H_x \quad (3.9)$$

Therefore, \mathbf{E} and \mathbf{H} are perpendicular. Taking \mathbf{E} in the x direction and \mathbf{H} in the y direction, equations 3.6 becomes an ordinary differential equation with solution:

$$\mathbf{E}_x(Z) = \mathbf{E}_0 e^{\pm ikz}; \quad \mathbf{H}_x(Z) = \mathbf{H}_0 e^{\pm ikz} \quad (3.10)$$

Where \mathbf{E}_0 and \mathbf{H}_0 are constants, the magnitude of \mathbf{E}_x and \mathbf{H}_y at $z=0$.

Using equation 3.7, the exponential of \mathbf{E} and \mathbf{H} can be expressed as:

$$\begin{aligned} e^{i(\omega t + kz)} &= e^{i(\omega t + i\sqrt{\frac{\mu\sigma\omega}{2}}Z - \sqrt{\frac{\mu\sigma\omega}{2}}Z)} \\ &= e^{-Z/\delta} e^{i(\omega t - \sqrt{\frac{\mu\sigma\omega}{2}}Z)} \\ &= e^{-Z/\delta} e^{i\omega(t - Z\sqrt{\frac{\mu\sigma}{2\omega}})} \end{aligned}$$

where

$$\sqrt{\frac{\mu\sigma}{2\omega}} = 1/v \quad (3.11)$$

Where v is the velocity of the propagating wave.

The plus sign in the exponent represents a wave propagation in the +z direction in the earth and exponentially decreasing in amplitude. The depth where the field has decreased to 1/e of its value at z=0 (the surface) is called the skin depth δ :

$$\delta = \frac{1}{\text{Im}(k)} = \frac{1}{\text{Im}(\sqrt{-i\mu\sigma\omega})} = \sqrt{\frac{2}{\mu\sigma\omega}} \quad (3.12)$$

It can be seen that the amplitude decreases for high conductivities and frequencies.

Using that $\mu = \mu_0 = 1.2566 \times 10^{-6}$ H/m and $\omega = 2\pi/T$, where T is the period of the incident field, a useful approximation for the skin depth is given by:

$$\delta = 500\sqrt{\rho T} \quad [\text{m}] \quad (3.13)$$

Equation 3.9 can be expressed in matrix form:

$$\begin{pmatrix} E_x \\ E_y \end{pmatrix} = \begin{pmatrix} 0 & Z_{xy} \\ Z_{yx} & 0 \end{pmatrix} \begin{pmatrix} H_x \\ H_y \end{pmatrix} \quad (3.14)$$

where

$$Z_{xy} = \frac{\mu\omega}{k} \quad \text{and} \quad Z_{yx} = -Z_{xy} \quad (3.15)$$

In the general case the horizontal components of the electric \mathbf{E} and the magnetic field \mathbf{H} are related via a complex impedance tensor \mathbf{Z} and can be presented as:

$$\begin{pmatrix} E_x \\ E_y \end{pmatrix} = \begin{pmatrix} Z_{xx} & Z_{xy} \\ Z_{yx} & Z_{yy} \end{pmatrix} \begin{pmatrix} H_x \\ H_y \end{pmatrix} \quad \text{or} \quad \mathbf{E} = \mathbf{Z}\mathbf{H} \quad (3.16)$$

\mathbf{Z} is a complex tensor, has both real and imaginary parts. Using $k = \sqrt{-i\mu\sigma\omega}$, we have

$$\mathbf{Z} = \frac{\mu\omega}{\sqrt{-i\mu\sigma\omega}} = \sqrt{i} \sqrt{\frac{\mu\omega}{\sigma}} = \sqrt{\frac{\mu\omega}{\sigma}} e^{i\pi/4} \quad (3.17)$$

By measuring \mathbf{E} and \mathbf{H} , we can determine the resistivity ρ

$$\rho = \frac{1}{\sigma} = \frac{1}{\mu\omega} \left| \frac{E_y}{H_x} \right|^2 = \frac{1}{\mu\omega} \left| \frac{E_x}{H_y} \right|^2 = \frac{1}{\mu\omega} |\mathbf{Z}|^2 \quad (3.18)$$

For a homogeneous earth, we can express the resistivity (ρ) and phase (ϕ) as:

$$\rho = \frac{1}{\mu\omega} |\mathbf{Z}|^2; \quad \phi = \arg(\mathbf{Z}) = \frac{\pi}{4} = 45^\circ \quad (3.19)$$

While for non-homogeneous earth we define the apparent resistivity (ρ_a) and phase (ϕ_a):

$$\rho_a = \frac{1}{\mu\omega} |\mathbf{Z}|^2; \quad \phi_a = \arg(\mathbf{Z}) \neq 45^\circ \quad (3.20)$$

On the surface of a 1-D layered earth (conductivity varies only with depth as presented in Figure 4), we have:

$$\begin{pmatrix} E_x(\omega) \\ E_y(\omega) \end{pmatrix} = \begin{pmatrix} 0 & Z_{xy}(\omega) \\ Z_{yx}(\omega) & 0 \end{pmatrix} \begin{pmatrix} H_x(\omega) \\ H_y(\omega) \end{pmatrix} \quad (3.21)$$

the diagonal elements of the impedance tensor are zero while the off-diagonal elements are equal in magnitude but have opposite signs ($Z_{xx}(\omega) = Z_{yy}(\omega) = 0$ and $Z_{xy}(\omega) = -Z_{yx}(\omega) = \hat{Z}_1$). The quantity of \hat{Z}_1 is determined by a recursion relations:

$$\hat{Z}_i = Z_i \frac{\hat{Z}_{i+1} + Z_i \tanh(ik_i d_i)}{\hat{Z}_i + Z_{i+1} \tanh(ik_i d_i)}; \quad i=N-1, \dots, 1 \quad (3.22)$$

where $Z_i = \mu\omega/k_i$ and $\hat{Z}_N = Z_N$

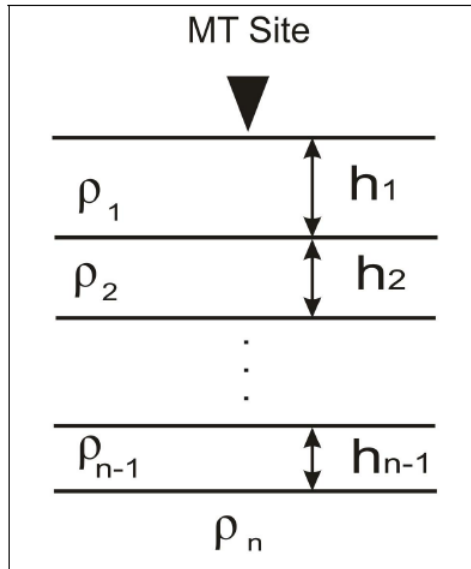


Figure 4. Simple 1-D layered earth model.

For a 2-D earth (conductivity varies in one horizontal direction and also with depth) measuring in the electrical strike direction, $Z_{xx}(\omega) \sim Z_{yy}(\omega) \sim 0$ and $Z_{xy}(\omega) \neq Z_{yx}(\omega)$. While for 3-D earth, $Z_{xx}(\omega) \neq Z_{yy}(\omega) \neq 0$ and $Z_{xy}(\omega) \neq Z_{yx}(\omega)$. Therefore, the impedance tensor \mathbf{Z} contains information about dimensionality. From our measured data, we can find out whether the resistivity structure could be approached by 1-D, 2-D or 3-D earth models, and therefore decide which inversion scheme should be performed, having the availability and reliability of the inversion algorithm in mind.

For 2-D electrical resistivity structure (Figure 5), the solutions of Maxwell's equations can be decoupled into two independent modes. One incorporating electric fields parallel to the electric strike and magnetic field components perpendicular to the strike and in the vertical plane (**E**-polarization, referred to as Transverse Electric (TE) mode) and the other incorporating magnetic fields parallel to the electric strike with induced electric field component perpendicular to strike and in the vertical plane (**B**-polarization, referred to as Transverse Magnetic (TM) mode).

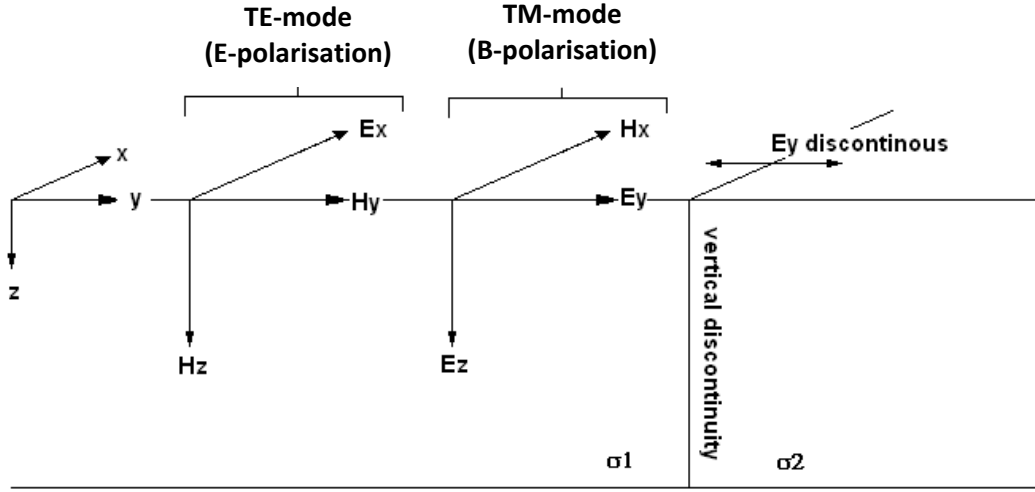


Figure 5. Simple 2-D model and the concept of polarization in magnetotellurics (after Simpson and Bahr, 2005)

Figure 5 shows a simple 2-D model composed of quarter-spaces with different conductivities, σ_1 and σ_2 , on each side of an infinite planar boundary in the strike direction (the x-direction). Conservation of charges means that the current density is continuous across the contact and the electric field in that direction must be discontinuous since $j_y = \sigma E_y$. In TE mode, E_x and H_z are continuous, vary smoothly across the discontinuity (Figure 5). In this case, ρ_{xy} which is proportional to E_x/H_y is smoothly varying across a discontinuity. While in TM mode, H_x and E_z component are continuous across the discontinuity but E_y is discontinuous. For TM mode the electric field is discontinuous at a discontinuity due to electric charge accumulation which is the underlying cause of the galvanic effect. Galvanic effect (distortion) is a non-inductive (frequency-independent) response of the electric field, which may distort MT impedance tensors. The two apparent resistivity values correspond to the modes mentioned above and can be written as:

$$\rho_{a,xy}(\omega) = \frac{1}{\mu\omega} \left| \frac{E_x(\omega)}{H_y(\omega)} \right|^2 \text{ for TE mode} \quad (3.23a)$$

and

$$\rho_{a,yx}(\omega) = \frac{1}{\mu\omega} \left| \frac{E_y(\omega)}{H_x(\omega)} \right|^2 \text{ for TM mode} \quad (3.23b)$$

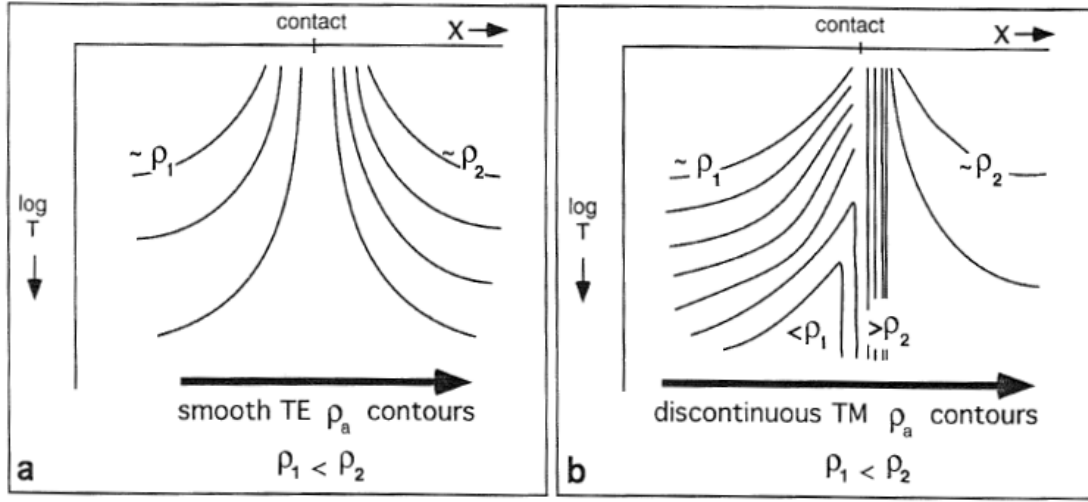


Figure 6. Transverse magnetic (TM) and transverse electric (TE) mode in magnetotellurics (Jiracek et al., 1995).

Theoretically, we can calculate the impedance tensor in any non-measured direction by rotating the measured impedance tensor using mathematical rotation through matrix multiplication. The rotational angle α , is represented by a rotation matrix R_α (see e.g. Vozoff, 1991):

$$R_\alpha = \begin{pmatrix} \cos \alpha & \sin \alpha \\ -\sin \alpha & \cos \alpha \end{pmatrix} \quad (3.24)$$

The rotated impedance tensor Z is given as:

$$Z' = R_\alpha Z R_\alpha^T \quad (3.25)$$

where the superscript T denotes the transpose matrix,

$$R_\alpha^T = \begin{pmatrix} \cos \alpha & -\sin \alpha \\ \sin \alpha & \cos \alpha \end{pmatrix} \quad (3.26)$$

And equation 3.25 can be expanded as:

$$\left. \begin{aligned} Z'_{xx} &= Z_{xx} \cos^2 \alpha + (Z_{xy} + Z_{yx}) \sin \alpha \cos \alpha + Z_{yy} \sin^2 \alpha \\ Z'_{xy} &= Z_{xy} \cos^2 \alpha + (Z_{xx} + Z_{yy}) \sin \alpha \cos \alpha - Z_{yx} \sin^2 \alpha \\ Z'_{yx} &= Z_{yx} \cos^2 \alpha + (Z_{yy} - Z_{xx}) \sin \alpha \cos \alpha - Z_{xy} \sin^2 \alpha \\ Z'_{yy} &= Z_{yy} \cos^2 \alpha + (Z_{yx} - Z_{xy}) \sin \alpha \cos \alpha - Z_{xx} \sin^2 \alpha \end{aligned} \right\} \quad (3.27)$$

3.2 Field measurement

The horizontal components of the electric field are measured on the surface of the earth using two pairs of electrodes (e.g. porous pots). The horizontal components and the vertical component of the magnetic field are measured on the surface of the earth as well by magnetic sensors (e.g. coils). The data are collected through a five channel MT data acquisition system. The electric field (E_x and E_y) is acquired by recording the time-varying potential difference between two non-polarizing electrodes on the surface, divided by their horizontal distance. While H_x , H_y and H_z are acquired by recording the magnetic induction in magnetic coils. The field layout is shown in Figure 7.

The MT data used in this study were collected by two groups. For our convenience we call the first data set, the “KMT – series”. They were measured by Duke University in 2004. Secondly, the so called “K – series”, measured by MSU (Moscow State University) and ÍSOR (Iceland GeoSurvey) in 2006. Most of these data are collected using five component systems. However, some of the K-series data were collected using two component systems measuring the electric field only. The magnetic field measured simultaneously at a nearby station was used in the processing of the data. One of the station in the K-series uses the magnetic field from a station at a distance of 3700 m (station K-81494) and stations K-81032 and K-81402 at a distance of 2500 m (the location of the stations is shown in Figure 9). These distances ought not to be larger than 1000 m, larger distances reduce the reliability of the results, in particular where large horizontal resistivity gradients are to be expected.

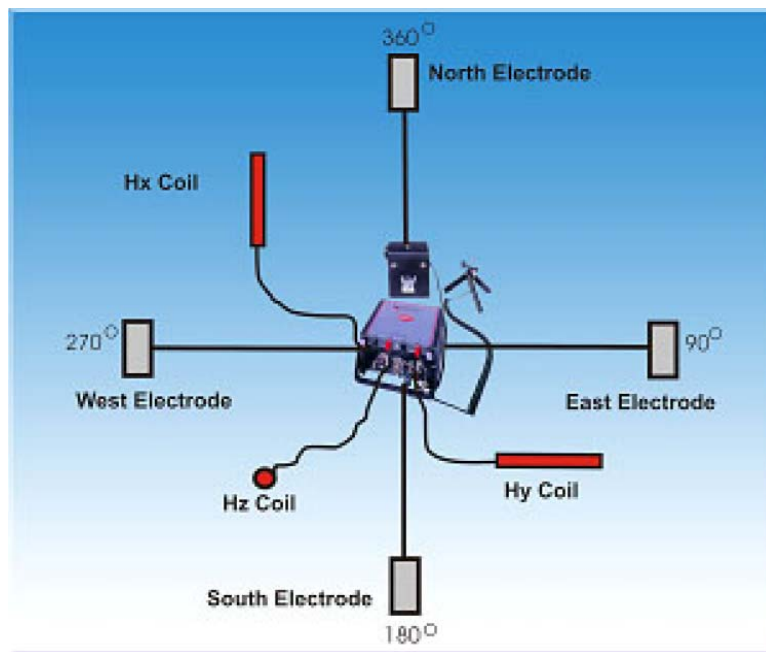


Figure 7. Field layout of a 5-channel MT data acquisition system.

The measuring x-direction was in the magnetic north, therefore when referring to geographical north the magnetic declination must be taken into account (the declination at Krafla is N14°W). From now on we will refer north to the geographical north and the impedances were rotated accordingly.

A remote reference MT station was set up 10 km away from the measuring or local sites. It was situated sufficiently far away from the local sites so that the cultural noise at both sites is uncorrelated. Thereby the signal to noise ratio of the local MT stations is increased. The remote reference stations are discussed separately in next chapter.

3.3 From time series to frequency domain

The electric and magnetic field time-variations of the MT data measurements are recorded as time series data (Figure 8A). However, we must keep in mind that the measured data not only contain the desired information, the signal, but also natural and/or cultural noises. Data processing in geophysics deals with reducing the noise from the measured data and increasing the signal-to-noise ratio. It includes the processing or reduction of the collected data to data that are ready for numerical

modelling. In magnetotellurics, the aim of data processing is to produce as smooth apparent resistivity curves as possible, as a function of frequency (or period) which represents the earth's response, and can be used to interpret the earth's subsurface conductivity structure. Although the data used in this study are in EDI file format (industry-standard file format of MT data of processed time series data) which was produced by MT data processing software from time series to frequency domain. The data processing in MT will be briefly discussed here.

Nowadays, most measured data are stored in digital form: virtually all collected MT data are amplified, filtered and digitized by an analog-digital converter of the instrument. The transformation from time domain to frequency domain is usually done by Fast Fourier Transform (FFT) (Vozoff, 1991).

The process is initiated by visual inspection of the measured data. Each station is checked for name, instrument channels, measurement direction, distance between the electrodes and other information. The time interval is initially chosen for performing the FFT, first calculating the Fourier coefficients and later reprocessed Discrete Fourier Transform into cross powers.

The cross power at one frequency f_j in the band f_{j-m}, f_{j+m} of two channels, says A_j and B_j can be calculated (see e.g. Vozoff, 1991) by:

$$\begin{aligned} \langle A(f_j), B(f_j) \rangle &= \frac{1}{2m+1} \sum_{k=j-m}^{j+m} A_k B_k^* \\ &= \langle A_j B_j^* \rangle, \text{ which will generally be complex.} \end{aligned} \quad (3.28)$$

The coherency of two channels at frequency f_j is defined as:

$$coh(A_j, B_j) = \frac{1}{2m+1} \sum_{k=j-m}^{j+m} \frac{A_k B_k^*}{\sqrt{(A_k A_k^*)(B_k B_k^*)}}, \quad (3.29)$$

which is complex with modulus between 0 and 1.

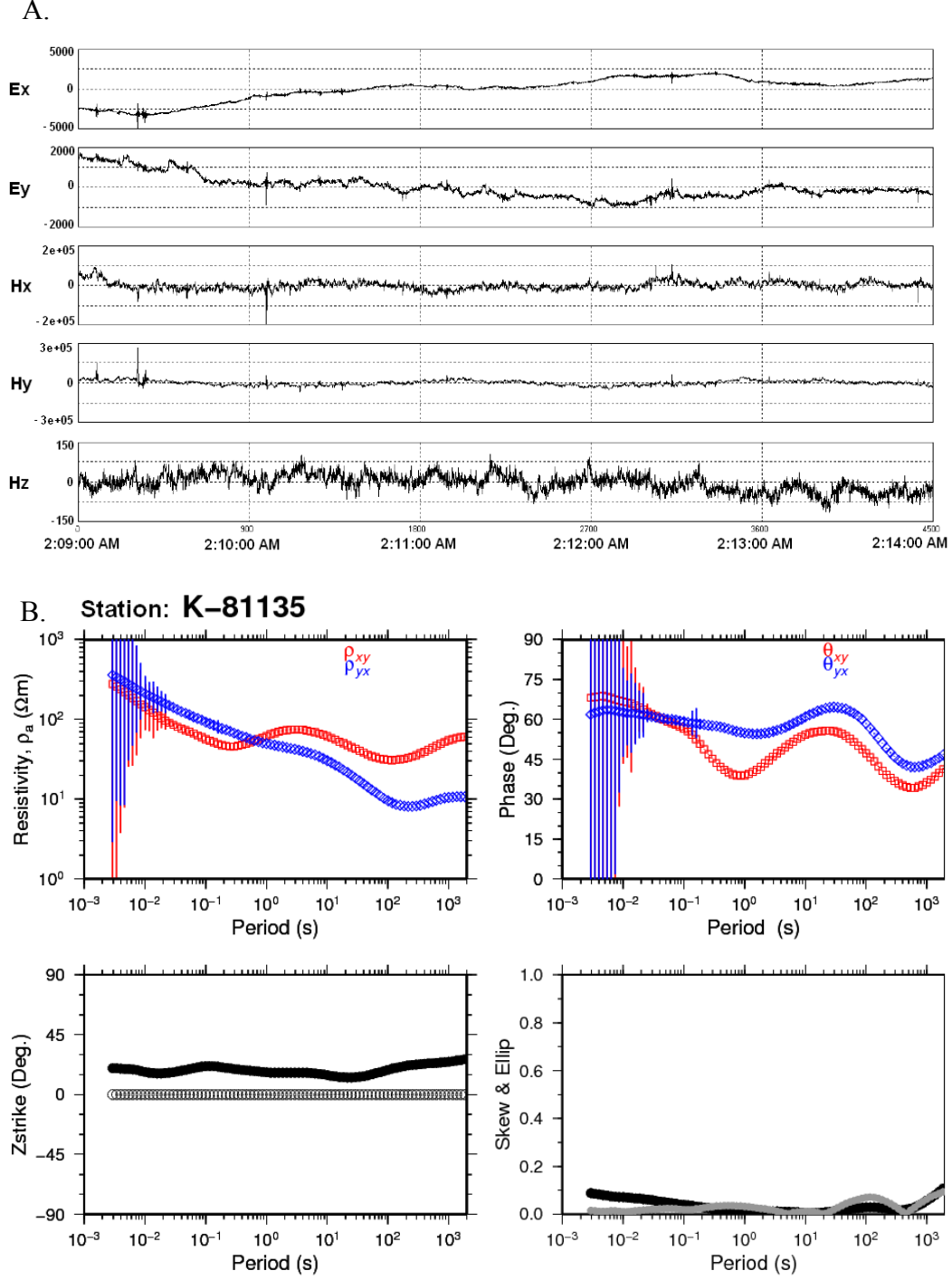


Figure 8. An example of magnetotelluric processing results. (A) Time series data acquired by a 5-channel MT data acquisition system; and (B) Apparent resistivity and phase curves calculated from the time series in (A) after processing the data. Also is shown as a function of period: the Swift angle or Zstrike to the right (note its constant value independent of the frequency, showing strong 2-D character) and to the left the ellipticity (grey dots) gives information on two dimensionality and the skew (black dots), gives information on three dimensionality.

Linear expansion of equation 3.16 gives:

$$E_x(\omega) = Z_{xx}(\omega)H_x(\omega) + Z_{xy}(\omega)H_y(\omega) \quad (3.30a)$$

$$E_y(\omega) = Z_{yx}(\omega)H_x(\omega) + Z_{yy}(\omega)H_y(\omega) \quad (3.30b)$$

multiplying by the complex conjugates of the electric and magnetic spectra gives the following equations:

$$\left. \begin{aligned} \langle (E_x(\omega)E_x^*(\omega)) \rangle &= Z_{xx}(\omega)\langle (H_x(\omega)E_x^*(\omega)) \rangle + Z_{xy}(\omega)\langle (H_y(\omega)E_x^*(\omega)) \rangle \\ \langle (E_x(\omega)E_y^*(\omega)) \rangle &= Z_{xx}(\omega)\langle (H_x(\omega)E_y^*(\omega)) \rangle + Z_{xy}(\omega)\langle (H_y(\omega)E_y^*(\omega)) \rangle \\ \langle (E_x(\omega)H_x^*(\omega)) \rangle &= Z_{xx}(\omega)\langle (H_x(\omega)H_x^*(\omega)) \rangle + Z_{xy}(\omega)\langle (H_y(\omega)H_x^*(\omega)) \rangle \\ \langle (E_x(\omega)H_y^*(\omega)) \rangle &= Z_{xx}(\omega)\langle (H_x(\omega)H_y^*(\omega)) \rangle + Z_{xy}(\omega)\langle (H_y(\omega)H_y^*(\omega)) \rangle \\ \langle (E_y(\omega)E_x^*(\omega)) \rangle &= Z_{yx}(\omega)\langle (H_x(\omega)E_x^*(\omega)) \rangle + Z_{yy}(\omega)\langle (H_y(\omega)E_x^*(\omega)) \rangle \\ \langle (E_y(\omega)E_y^*(\omega)) \rangle &= Z_{yx}(\omega)\langle (H_x(\omega)E_y^*(\omega)) \rangle + Z_{yy}(\omega)\langle (H_y(\omega)E_y^*(\omega)) \rangle \\ \langle (E_y(\omega)H_x^*(\omega)) \rangle &= Z_{yx}(\omega)\langle (H_x(\omega)H_x^*(\omega)) \rangle + Z_{yy}(\omega)\langle (H_y(\omega)H_x^*(\omega)) \rangle \\ \langle (E_y(\omega)H_y^*(\omega)) \rangle &= Z_{yx}(\omega)\langle (H_x(\omega)H_y^*(\omega)) \rangle + Z_{yy}(\omega)\langle (H_y(\omega)H_y^*(\omega)) \rangle \end{aligned} \right\} \quad (3.31)$$

Most of these equations contain autopowers, which amplify the correlated noise presented in the data and causing Z_{ij} to be biased. The incoherent noise in the measured electric fields will bias the estimated Z_{ij} upwards while the incoherent noise in the measured magnetic fields will bias the estimated Z_{ij} downwards. One known method to solve this problem is to deploy a remote reference site (Gamble et al., 1979a, 1979b) at a distance sufficiently away from the measuring or local site so that it can be presumed that the noise is uncorrelated. Then replacing all the complex conjugates in eq. 3.31 (denoted*) with the remote site components, giving the equations:

$$Z_{xx} = \frac{\langle E_x R_x^* \rangle \langle H_y R_y^* \rangle - \langle E_x R_y^* \rangle \langle H_y R_x^* \rangle}{\langle H_x R_x^* \rangle \langle H_y R_y^* \rangle - \langle H_x R_y^* \rangle \langle H_y R_x^* \rangle} \quad (3.32a)$$

$$Z_{xy} = \frac{\langle E_x R_x^* \rangle \langle H_x R_y^* \rangle - \langle E_x R_y^* \rangle \langle H_x R_x^* \rangle}{\langle H_y R_x^* \rangle \langle H_x R_y^* \rangle - \langle H_y R_y^* \rangle \langle H_x R_x^* \rangle} \quad (3.32b)$$

$$Z_{yx} = \frac{\langle E_y R_x^* \rangle \langle H_y R_y^* \rangle - \langle E_y R_y^* \rangle \langle H_y R_x^* \rangle}{\langle H_x R_x^* \rangle \langle H_y R_y^* \rangle - \langle H_x R_y^* \rangle \langle H_y R_x^* \rangle} \quad (3.32c)$$

$$Z_{yy} = \frac{\langle E_y R_x^* \rangle \langle H_x R_y^* \rangle - \langle E_y R_y^* \rangle \langle H_x R_x^* \rangle}{\langle H_y R_x^* \rangle \langle H_x R_y^* \rangle - \langle H_y R_y^* \rangle \langle H_x R_x^* \rangle} \quad (3.32d)$$

where R_x and R_y represent H_x and H_y of remote site components, respectively. It is sometimes more convenient to use pair of E -field receivers.

The FFT process generally yields much more frequencies than can be used for the interpretation, especially of higher frequency. In order to provide smoother results and reduce the number of data after the FFT process, one approach is to average the impedance values over adjoining groups of frequencies or windows. Within this process, robust processing can be applied to reduce the size of error bars and smooth the curves in plots of apparent resistivity.

In robust processing, the evaluation of individual data point is performed to calculate the data average and down-weighting the outliers and therefore narrow the average value in the stacking process. In many cases with high noise effects, the apparent resistivity curves remain not as smooth as we expected despite the application of the robust processing. In this problem, manual editing of the stacked apparent resistivity value for each frequency is needed to produce reasonable results and smoother apparent resistivity curves. Example of resulting apparent resistivity and phase with their attributes are presented in Figure 8B.

4 MT data

4.1 MT apparent resistivity and phase

The MT data used in this study consist of 39 measuring sites which were collected by two groups on three profiles within the Krafla caldera (Figure 9). Two profiles (AV7290 and AV7288) are used for 1-D and 2-D modelling, while KRF-2 is used only in 1-D inversion.

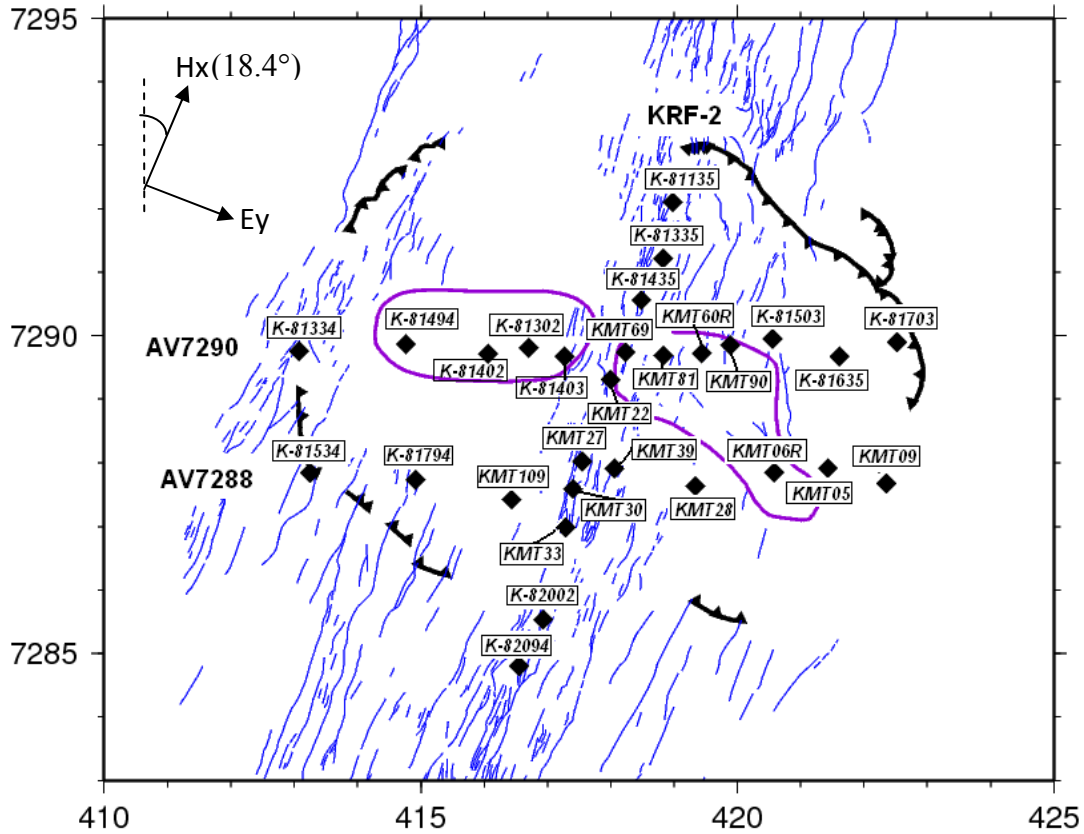


Figure 9. Location of the MT soundings and the MT profiles used for 1-D and 2-D inversion: AV7290 and AV7288, and profile KRF-2, used for 1-D inversion only. X-axis is N18.4°E in definition of the modes and representing the preferred geoelectrical structure in the area. Two S-wave shadow zones from Einarsson (1978) are presented by the purple lines, blue lines denote the main fractures and black bold lines are the rim of the caldera.

These two series of data have periods ranging from 0.003 to 2000 s and on the average 78 to 90 periods for each site. Although they have the same range of periods, both data series are sampled in the different periods. In order to run 2-D inversion using REBOCC code (Siripunvaraporn and Egbert, 2000), which requires uniform periods for all sites within the profile, data have been resampled to make uniform series of periods ranging from 0.01 to 1000 s and covering 10 frequencies per decade with a total of 50 periods (Figure 10).

Station: K-81794

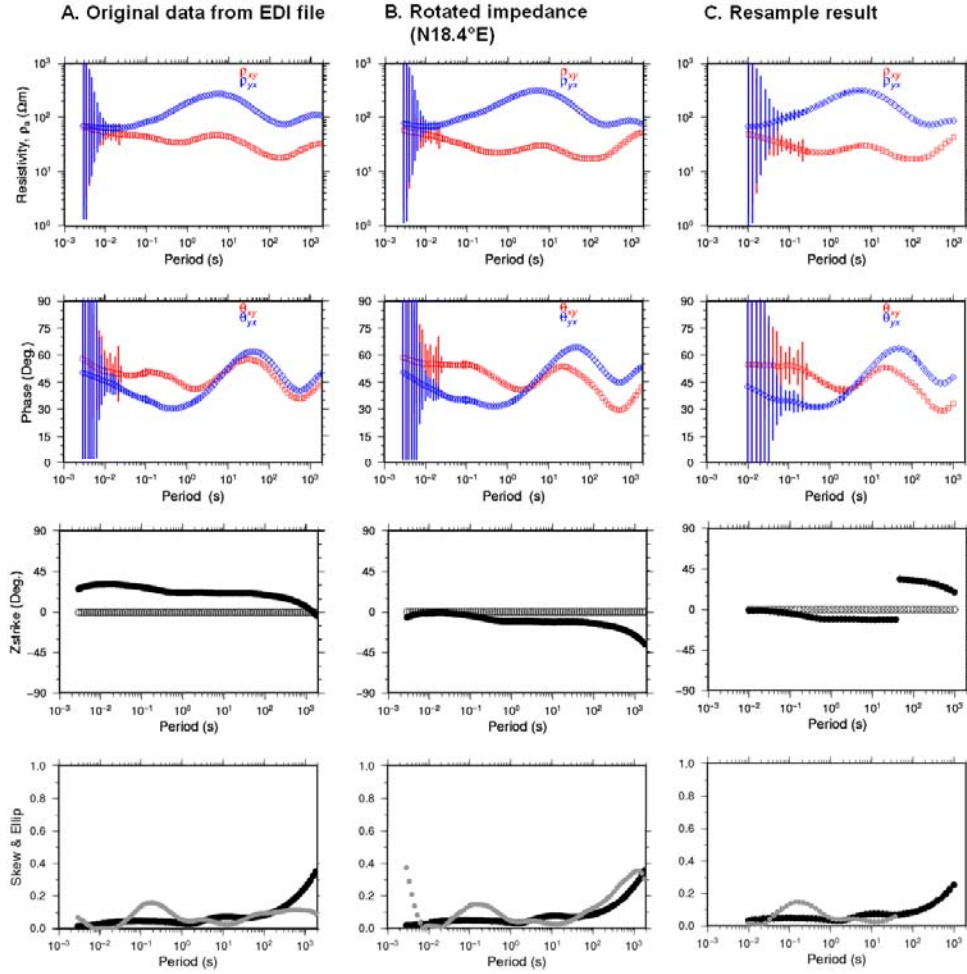


Figure 10. Example of resampled MT data. The plot to the right (C) has 50 resampled periods ranging from 0.01 – 100 s after rotation of 18.4°, shown in (B). While (A) is the original data before rotation. The rows show as a function of the period: the apparent resistivity, the impedance phase, Swift's strike (Zstrike) and the skew and ellipticity, respectively.

All the data collected in profiles AV7290 and AV7288 are presented as apparent resistivity and impedance phase pseudo-sections for both transverse magnetic (TM) and transverse electric (TE) mode (Figure 11). These pseudo-sections are useful for highlighting the anomalies and summarizing the result. Difference between the TE and TM mode are expected in the data except for 1-D response due to the different sensitivity of the modes because of the earth's electrical structure especially near a vertical contact (Roy et al., 2004). However, we are emphasizing the TM mode in our analysis since the TM mode is relatively sensitive to the west-east variation (along the profile), while the TE mode is relatively sensitive to the north-south variation of resistivity.

The quality of the data is very good as reflected by the smooth apparent resistivity and phase curves and in particular does not suffer the dead band problem (at frequency around 1 Hz) where the signal is commonly weak. The apparent resistivity and phase curves with corresponding error bars in Figures 8 and 10 represent the data quality as the result of the robust processing implemented in the MT data processing.

A. AV7290

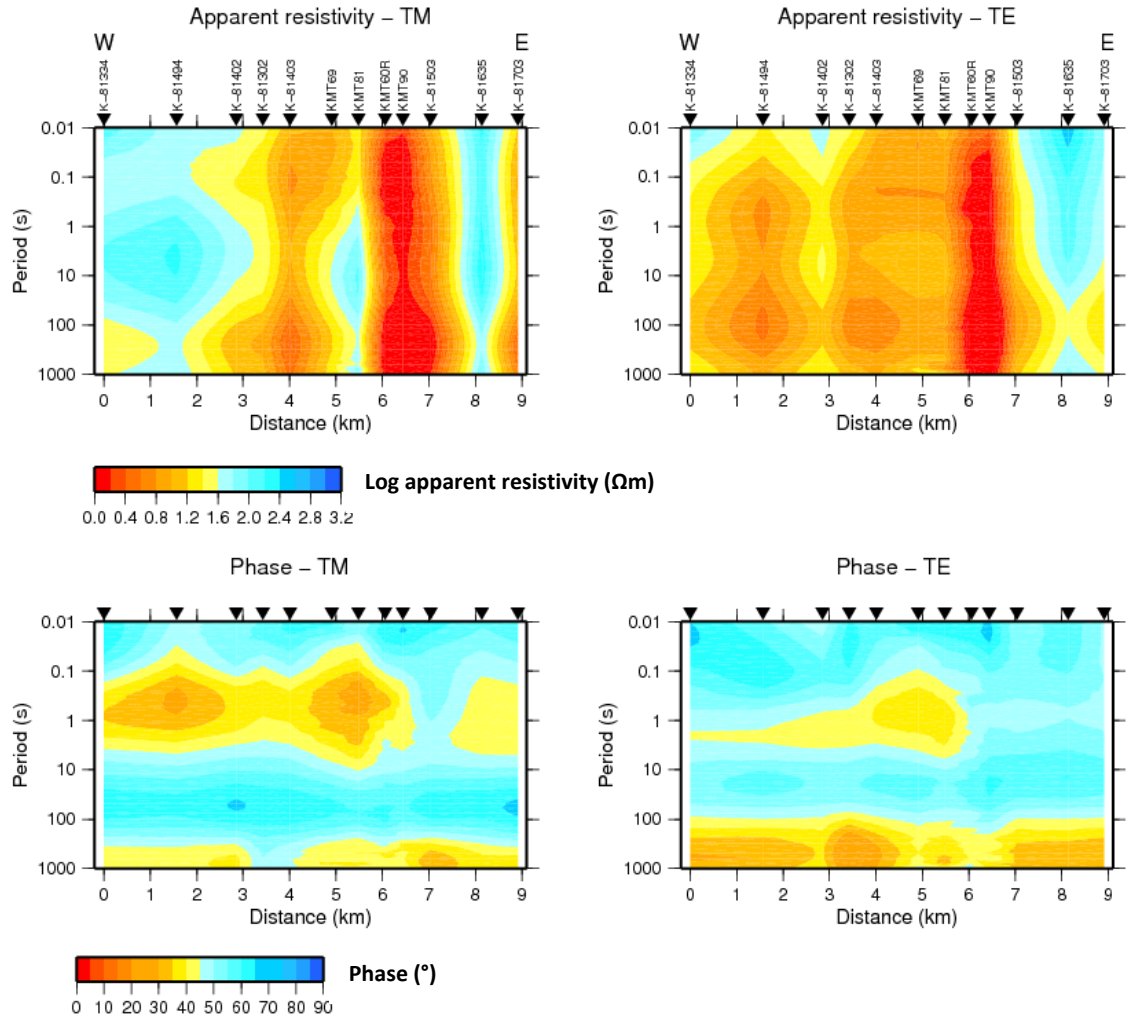


Figure 11. Apparent resistivity and phase pseudo-sections of MT TM and TE modes. (A) profile AV7290 and (B) profile AV7288.

B. AV7288

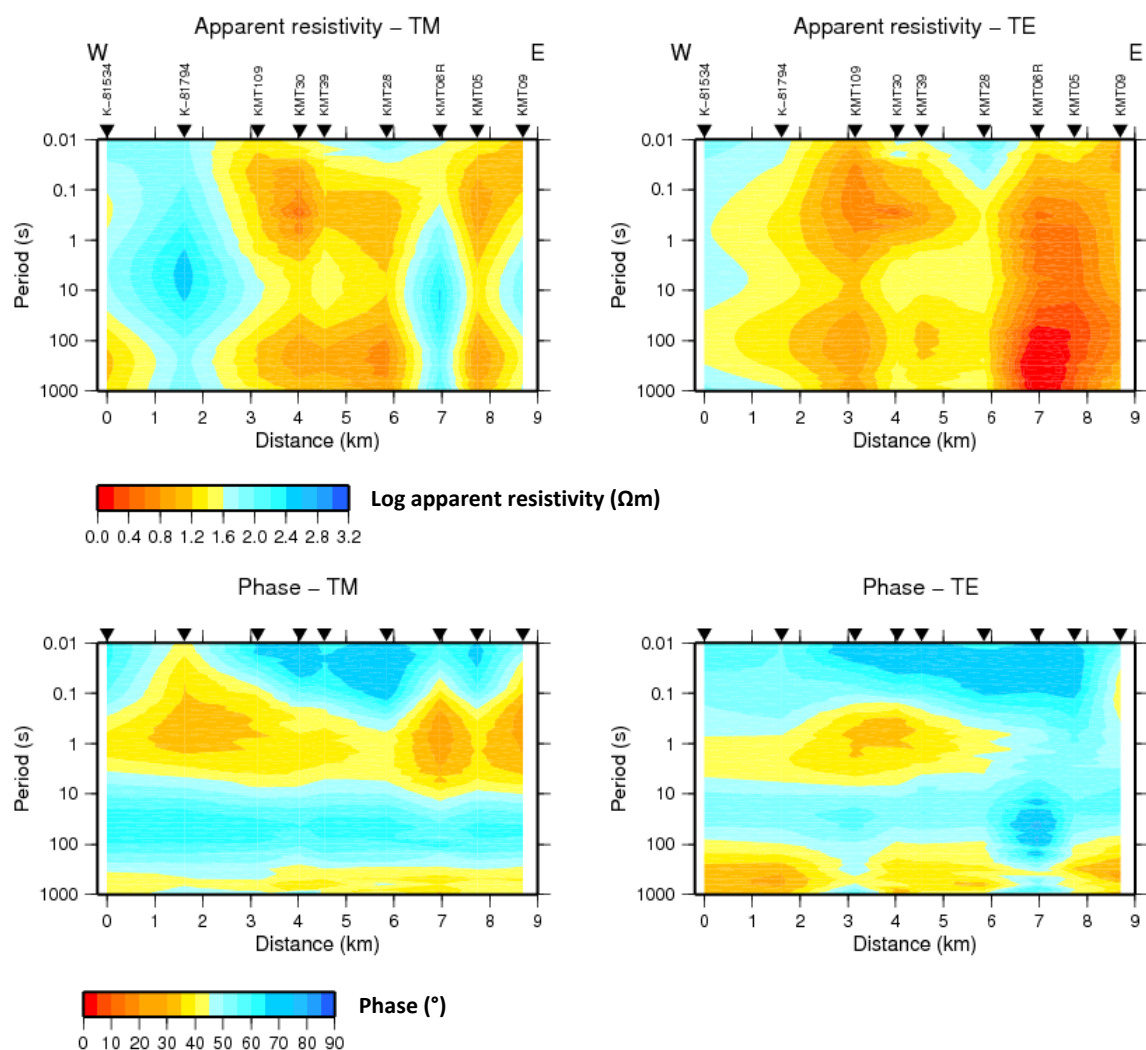


Figure 11. (continued).

The MT data exhibit regional complexities which can be seen over the entire range of periods (the dimensionality will be discussed in next chapter). The apparent resistivity and phase curves are split for all sites at longer periods. Several sites even show high splitting starting at short periods.

From the apparent resistivity distribution, the average resistivity within the Krafla caldera seems to be less than $20 \Omega m$, with some high values at its flanks (Figure 11) and very low (less than $1 \Omega m$) in the center of the caldera.

The splitting at short periods is also noticed in almost all of the data due to the shallow distortion known as “static-shift” problem. The static shift has been a common problem in geothermal areas in volcanic environment (high near surface resistivity contrast). In order to overcome the static shift problem we used TEM data to correct for the static shift and did 1-D joint inversion of the TEM and MT data.

Because the static shift is independent of the frequency it should not affect the phase. It is necessary to observe the phase since it is one of the most important MT parameter and also unaffected by the static shift. Along both profiles, the TE mode has a low phase values ($30^\circ - 40^\circ$) at short periods ($0.1 - 10$ s) within the western and

central part of the caldera whereas smaller lateral variations in TM impedance phase are observed across the caldera along the southern profile.

Along the northern profile (AV7290), sharp lateral apparent resistivity variations appear in both modes beneath the eastern portion of the caldera (below Viti). This is the result of the very low apparent resistivity values at sites KMT60R and KMT90. Furthermore, TEM measurements suggest that these two sites are highly shifted downwards by a factor 0.1 - 0.2 of normal scale resulting in very low measured apparent resistivity.

At sites K-81403 and KMT69, low resistivity values were doming up to the surface, coinciding with the NNE fissure swarm and indicating that our preferred rotational angle is correct for both profiles.

4.2 Dimensionality and strike direction

Various techniques have been developed to determine the dimensionality of the electrical conductivity structure. One of these techniques is the Swift's skew parameter (Swift, 1967). The Swift's skew (κ) is a rotationally invariant misfit parameter which is defined as the ratio between the magnitudes of the diagonal and the off-diagonal elements of the impedance tensor:

$$\kappa = |Z_{xx} + Z_{yy}| / |Z_{xy} - Z_{yx}| \quad (4.1)$$

In Figure 12, the Swift's skew values of the data are generally less than 0.2 which indicate either 1-D or 2-D resistivity structure of the area. Increasing skew values with increasing periods (e.g. sites K-81703 and K-81503 on profile AV7290 and sites KMT06R and KMT09 on profile AV7288) indicate 3-D behavior. Increasing skew values from 1 s to the longest period were also noticed in almost all the sites. However, Swift's skew is not a recommended parameter for identifying the dimensionality of the data when the 3-D heterogeneities that cause non-inductive distortion affects the MT data.

Recently, Caldwell et al. (2004) proposed the concept of magnetotelluric phase tensor as a means of recognizing the dimensionality of MT data. The phase relationship between the electric and magnetic field vector will be virtually unaffected if the distortion is galvanic.

The Swift's strike direction (θ_0) at which $|Z_{xx}(\theta_0)|^2 + |Z_{yy}(\theta_0)|^2$ is minimised (for simple 2-D case) can be calculated through:

$$\tan 4\theta_0 = \frac{2\text{Re}(S'_2 D'_1)}{|D'_1|^2 - |S'_2|^2} \quad (4.2)$$

where

$$D'_1 = \cos^2 \theta_0 (Z_{xx} - Z_{yy}) + \sin^2 \theta_0 (Z_{xy} + Z_{yx}) \quad (4.3)$$

$$S'_2 = \cos^2 \theta_0 (Z_{xy} + Z_{yx}) - \sin^2 \theta_0 (Z_{xx} + Z_{yy}) \quad (4.4)$$

The computed strike direction contains a 90° ambiguity because rotation by 90° only changes the location of the principal impedance tensor elements within the tensor:

$$\begin{aligned} R_{90} \begin{pmatrix} 0 & Z_{xy} \\ Z_{yx} & 0 \end{pmatrix} R_{90}^T &= \begin{pmatrix} 0 & 1 \\ -1 & 0 \end{pmatrix} \begin{pmatrix} 0 & Z_{xy} \\ Z_{yx} & 0 \end{pmatrix} \begin{pmatrix} 0 & -1 \\ 1 & 0 \end{pmatrix} \\ &= \begin{pmatrix} 0 & -Z_{xy} \\ -Z_{yx} & 0 \end{pmatrix} \end{aligned} \quad (4.5)$$

where R_{90} is a rotation matrix at 90° and T denotes the transpose matrix.

Figure 13 shows Swift's strike direction for all periods and all the measuring sites in the Krafla caldera.

At short periods (top left of Figure 13), the orientations of strike directions are diverging to several directions. This could be the effect of either 90° ambiguities or the 3-D environment at shallow depth. Even so, in the center of the caldera along the highly fractured area, the strike directions follow the average orientation of the fissure swarm. The changing orientations of the strike direction between each station can be seen at the periods ranging between 1 to 100 s which indicates the 3-D effect at different depth. This occurrence appeared in site K-81302 where at the shorter periods the preferred direction is oriented to the NE but at longer periods the highest changes are rotated following the NNE orientation. Interesting strike direction affected by another structure and 90° ambiguity can also be seen at site K-81534. On average, the preferred strike direction for this site is following the shape of the eastern caldera rim and it is highly affecting the data. As for K-81534, the presence of ambiguity can also be found at the period range of 1 to 100 s with preferred direction of 90° from the direction of the structure of the caldera rim.

For the longest periods the orientation is mostly the same and varies insignificantly compared to the changes between the two previous shorter periods. It is reflecting the reduction of the complexity of the area at greater depth. At this range all the stations have an orientation in the NNE direction on average except for a few stations. As an average direction for all the periods (bottom right of Figure 13) the preferred electrical strike direction is more or less following the orientation of the main geological structure that can be found on the surface (i.e. N14.8°E).

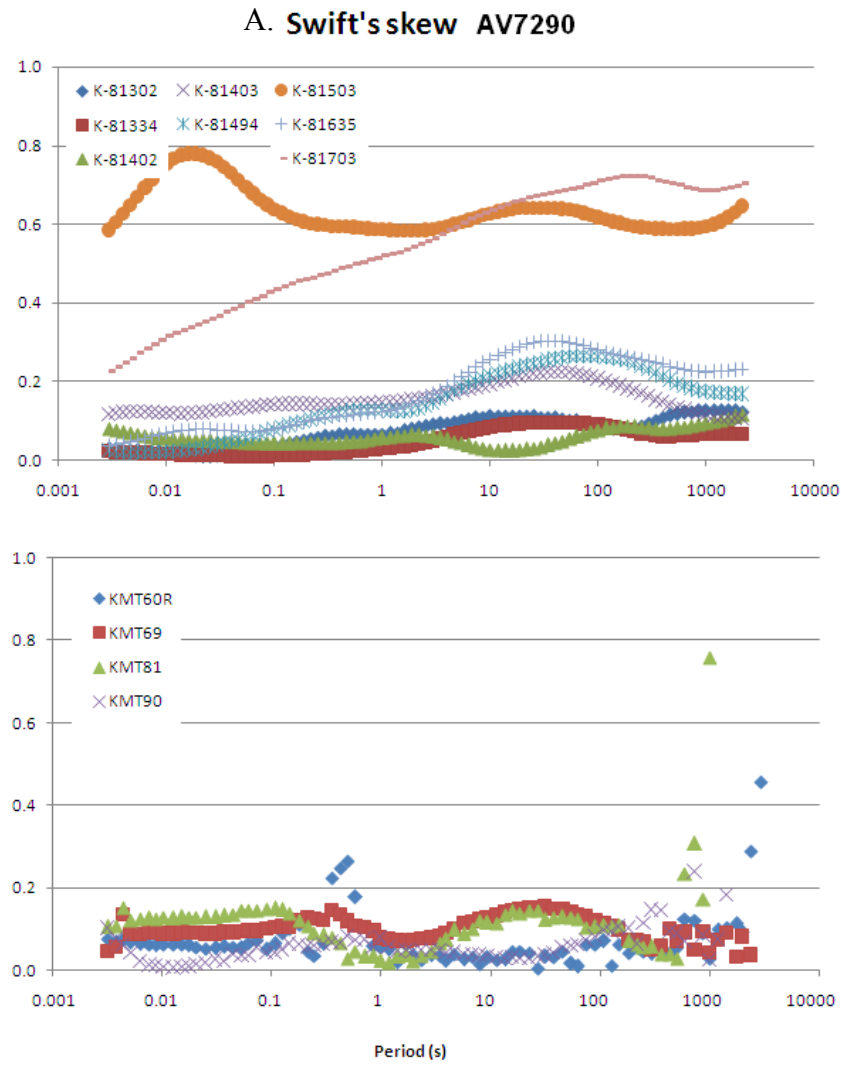


Figure 12. A. Swift's skew value for all sites on profile AV7290

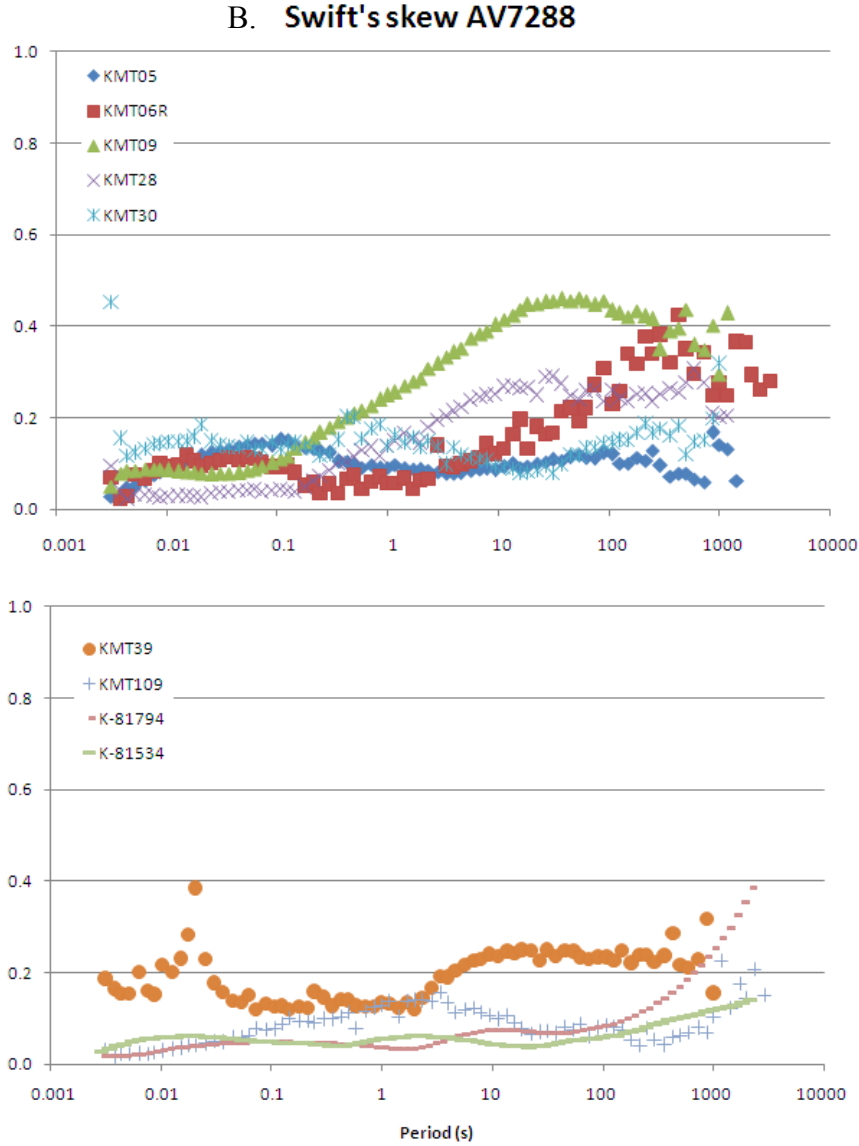


Figure 12. B. Swift's skew value for all sites on profile AV7288.

4.3 Static shift correction

The MT method and all resistivity methods that are based on measuring the electric field on the surface suffer a telluric or static shift problem, while those using the magnetic field only are relatively unaffected. Conductivity discontinuity close to the electric dipoles is one of the reasons for this problem. Originally, in the derivation of the diffusion equation (eq. 3.2a and 3.2b) we assumed $\nabla \cdot \mathbf{E}$ to be zero which means that the electrical charges are neglected, but when the current crosses a discontinuity it will build up electrical charges along the discontinuity. This will distort the electric field and cause the impedance magnitude to increase or decrease by real scaling factor and therefore shift the apparent resistivity curve up or down on log scale.

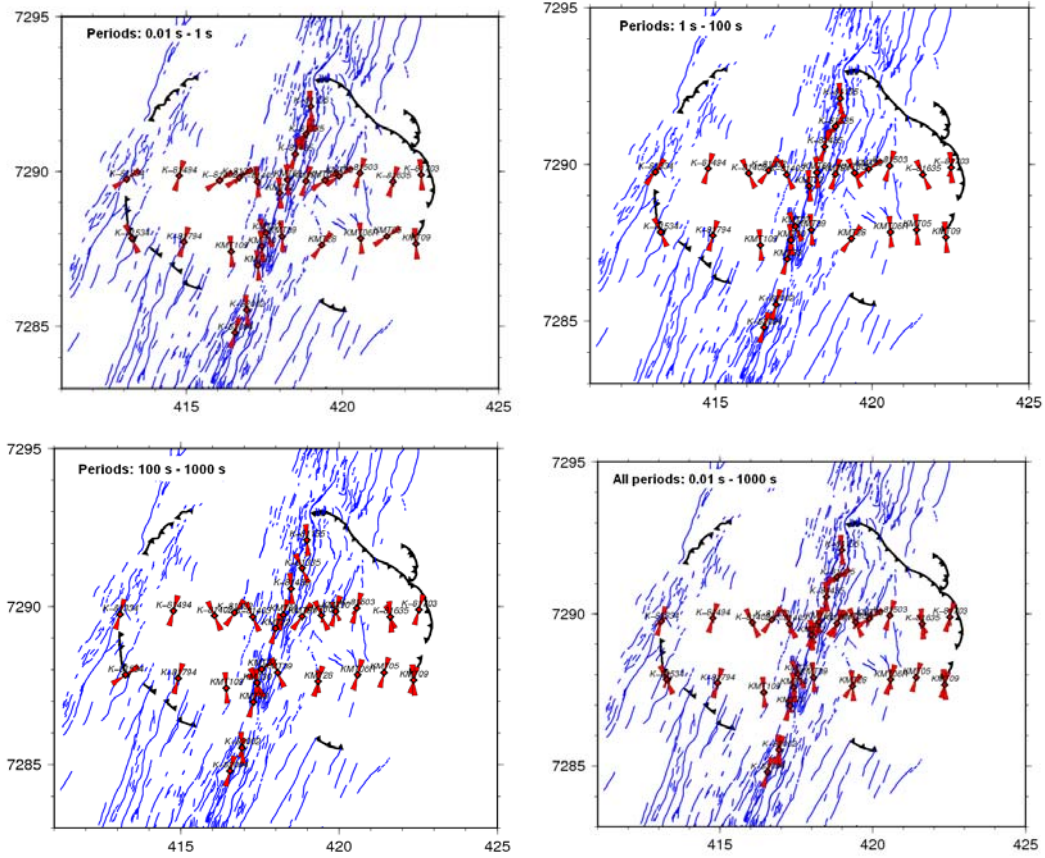


Figure 13. Preferred strike direction of each MT site (red) overlies the fissure swarm (blue lines) derived from Swift's equation for four different periods (name of the MT sites can be seen clearly in Figure 9). Caldera rim is presented in hedge black lines.

Figure 15 in chapter 5.2 shows how the static shift problem affects the model in 1-D inversion and may lead to misinterpretation of the resistivity structure. This parallel shift in the apparent resistivity curve is independent of the frequency and therefore it does not affect the impedance phase.

This problem can lead to incorrect interpretations of MT data if not taken seriously. Sternberg et al. (1988) illustrate how the static shift is produced by shallow inhomogeneities and came with the solution for this problem. One of the solutions to the static shift problem is to invert jointly the central-loop Transient Electro-Magnetic (TEM) and MT data, because TEM does not suffer the static shift problem.

TEM uses a loop of wire on the ground transmitting a constant current through it and thereby building up a magnetic field with known strength. The current is then abruptly turned off and the magnetic field induces currents in the ground. Due to Ohmic heat loss, the current and the magnetic field will decay and induce currents at greater depth (Figure 14). The decay rate of the magnetic field depends on the current distribution which in turn depends on the resistivity distribution. The resistivity structure of the subsurface can be obtained by measuring the induced voltage in a coil at the surface. The results are normally expressed as late apparent resistivity:

$$\rho_a(t) = \frac{\mu_0}{4\pi} \left| \frac{2\mu_0 I A_r A_s}{5t^{5/2} V(t)} \right|^{2/3} \quad (4.6)$$

where $\rho_a(t)$ is the apparent resistivity as a function of time after the current turned off (also called the late time apparent resistivity), $V(t)$ is the induced voltage at time t , I is the current strength, A_r and A_s are the effective area of the receiver coil and the source loop, respectively and μ_0 is the magnetic permeability of vacuum.

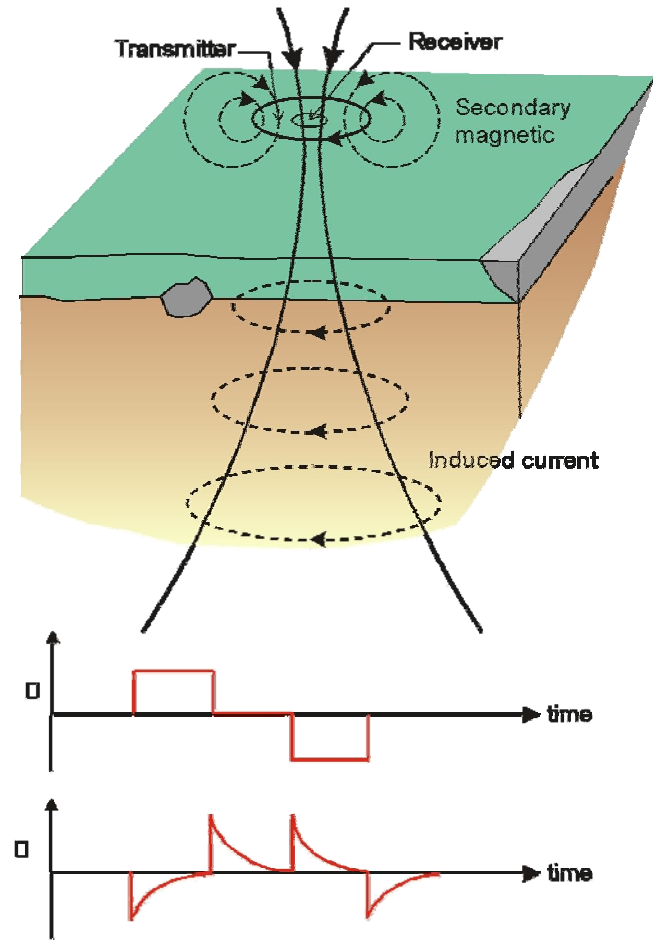


Figure 14. TEM sounding setup, transmitted current and measured transient voltage (Hersir and Björnsson, 1991).

In the TEM method, the current distribution at late time has diffused deep below near surface inhomogeneities and the effect of near surface resistivity inhomogeneities disappears. Therefore, the TEM/MT joint inversion has become the best approach to solve this problem so far (chapter 5.2).

In 2-D interpretation, the static shift correction has to be applied separately for each mode (shift multiplier S_{xy} applied to TE mode and S_{yx} to TM mode).

5 1-D MT data inversion

5.1 The 1-D MT inversion

To interpret MT data, forward and inversion scheme are commonly used in order to find the best fitted resistivity structure. For N-layered earth model, we used the TEMTD program (Árnason, 2006) to perform inverse modelling.

The inverse problem is solved to retrieve a representative model of the subsurface from measured data, while the forward problem is solved by calculating the response from a given model. The forward algorithm used in this program is a standard complex impedance 1-D recursion algorithm, while the Levenberg-Marquardt non-linear least square inversion is used in the program to solve the inversion problem. The root mean square (RMS) difference between measured and calculated values is weighted by the standard deviation of the measured values.

In order to prevent over-interpretation of the data, the program also includes the Occam inversion scheme to produce „smooth“ structure (or ‘least-structure’ model). In this process the program tries to find the smoothest model with many layers of fixed thickness that fits the data with the acceptable threshold tolerance instead of fitting the measured data as well as possible (Constable et al., 1987).

Besides the Occam inversion scheme, the program also offers the possibility of keeping the model smooth, both with respect to resistivity variations between layers (logarithm of conductivities) and layer thicknesses (logarithm of the ratio of the depth to top and bottom of layers) as shown in Figure 15.

In the inversion method, many models can generate good fit to the data. Because the electromagnetic energy propagates diffusively, MT soundings produce gradual conductivity changes rather than sharp boundaries or thin layers. Therefore, the philosophy of minimizing model complexity is valid. However, another a priori data should be used in conjunction to interpret the resistivity model produced from the inversion.

5.2 TEM-MT joint 1-D inversion

To overcome the static shift problem as described in the previous chapter, we carried out the TEM/MT joint inversion for each MT sounding. The location of TEM stations in Krafla are close to the corresponding MT station (within 200 m) so that they can be used with the MT soundings to do a joint inversion.

The forward algorithm of the TEM uses recurrence relations to calculate the kernel function for the vertical magnetic field due to an infinitesimal grounded dipole with harmonic current on the surface of horizontally layered earth (Árnason, 1989).

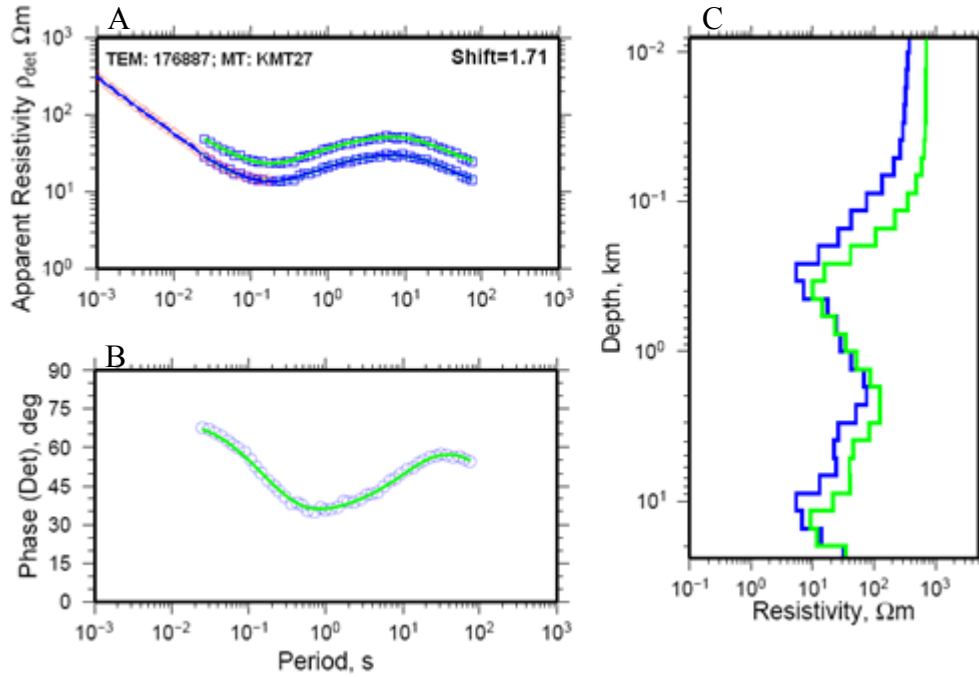


Figure 15. An example of 1-D TEM/MT joint inversion. The apparent resistivity curve in A shows the measured and calculated data before it is corrected by static shift (green line), while the curve below (calculated apparent resistivity in blue line) represents the result of TEM/MT joint inversion. The MT station (KMT27) is jointly inverted with TEM station 176887. In B apparent phase curves are unaffected by the static shift problem. The corresponding models to the calculated apparent resistivity and phase is shown in C, where the model with the green line is calculated from the uncorrected curve and the blue line after the static shift correction. In this example, the static shift factor is 1.71 on linear scale.

5.3 1-D resistivity model of Krafla

Two of the 1-D cross sections (AV7290 and AV7288) are the same as the ones in Árnason et al. (2009). For each cross section, the rotationally invariant determinant apparent resistivity and phase of MT data are jointly inverted with its corresponding TEM site (Figure 15) using Occam inversion as discussed in section 5.1. Since we have all the components of the impedance (Z_{xx} , Z_{yx} , Z_{xy} and Z_{yy}) of our data, we use the determinant value in the 1-D layered earth inversion. The advantage of using the determinant data is that it provides a useful average of the impedance for all current directions. The results are presented in Figures 16 to 18.

In general, these three profiles represent the conductivity structure within the Krafla caldera. The uppermost conductor consists of a relatively thin low resistivity layer associated with hydrothermal alteration, beneath a highly resistive near-surface cover. The uppermost 5-7 km within the caldera are characterized by increasing resistivity with depth between two prominent low-resistivity domes merging with a horizontal low-resistivity layer at 7-15 km depth. The top of the high-resistivity core below the shallow low resistivity layer is associated with high temperature alteration (Árnason et al., 2000). The deeper conductor at ~7 km depth appears with varying thickness. For profile AV7290, the deeper conductor domes up at the shallower depth below Leirhjúkur and Víti crater which are both located within the fissure swarm. Two low-resistivity domes are also present on the southern profile, AV7288 (Figure 17)

originating from a mid-crustal layer at 9-10 km depth. The eastern anomaly has a similar magnitude as the domes along the northern profile whereas the western anomaly is not visible above 5 km depth. The eastern dome is discontinuous above 5 km depth.

The low-resistivity domes correlate very well with the shear wave attenuation zones delineated by Einarsson (1978) and is interpreted as containing partial melt. The northern profile crosses both zones (Figures 2 and 9) whereas the southern profile crosses the SE stretching tail of the eastern shear wave attenuation zone.

A third profile, KRF-2 (Figure 18) parallel to the NNE-SSW trending fissure swarm and crossing the region between the two shear wave attenuation zones, is characterized by a broad 'up-doming' anomaly narrowing upwards, from 10 km depth beneath the southern caldera rim. The southern caldera region was subjected to rifting events in 1977 and 1980 during which dike intrusions propagated along the fissure swarm at shallow depth. This region was also seismically active during inflation periods (Figure 2) reflecting its proximity to the region of magma accumulation. Interconnected melt in the form of a cooling dike complex may thus still be present within the southern part of the caldera. However, this conductive dome is more likely to represent a near-vertical caldera fault zone rather than lateral dike intrusions. As along the EW profiles, near-surface low-resistivity anomalies coincide with surface geothermal areas and may be associated with hydrothermal activities.

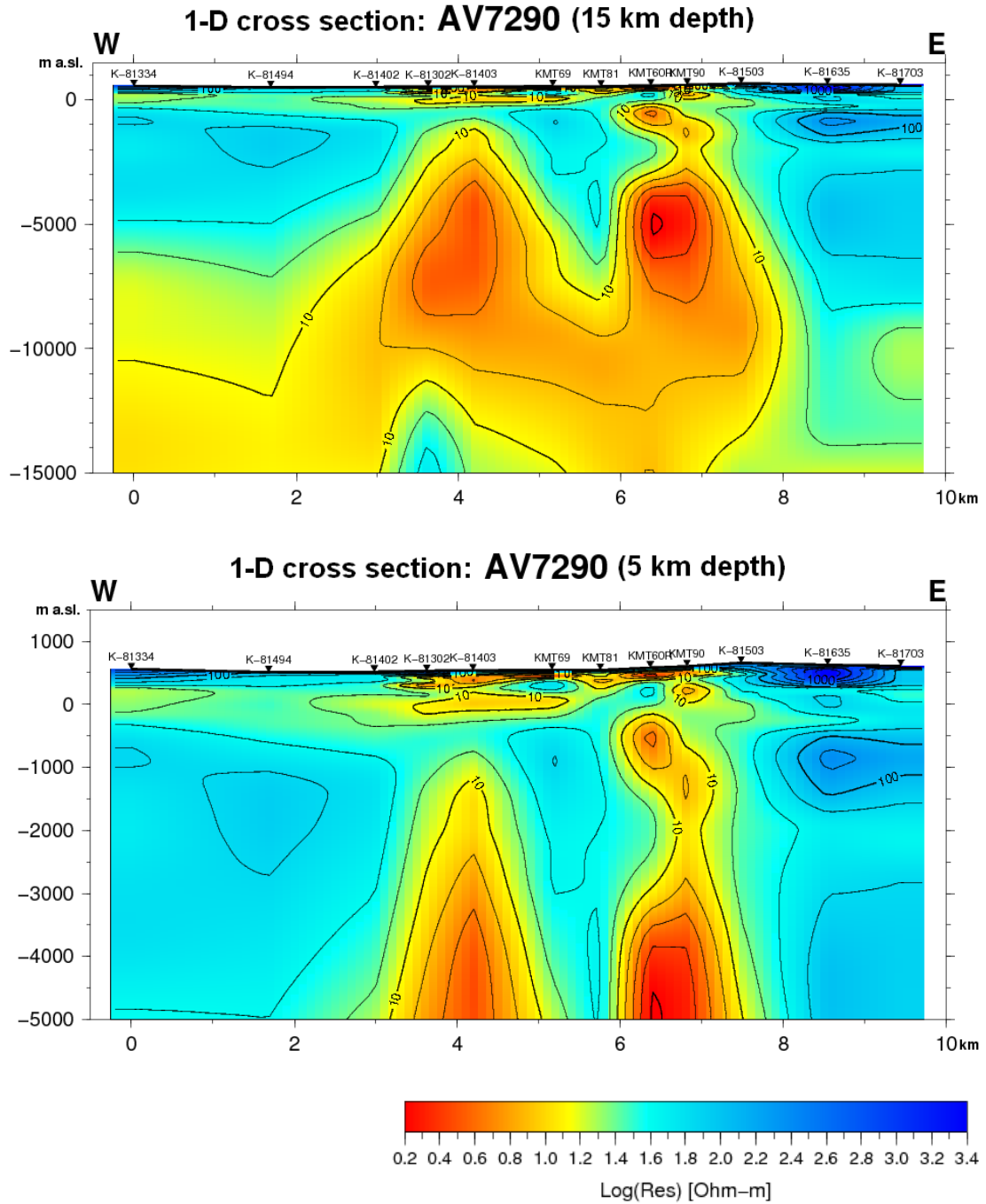


Figure 16. 1-D resistivity cross sections of MT soundings on profile AV7290, 15 km depth (Top) and 5 km depth (Bottom).

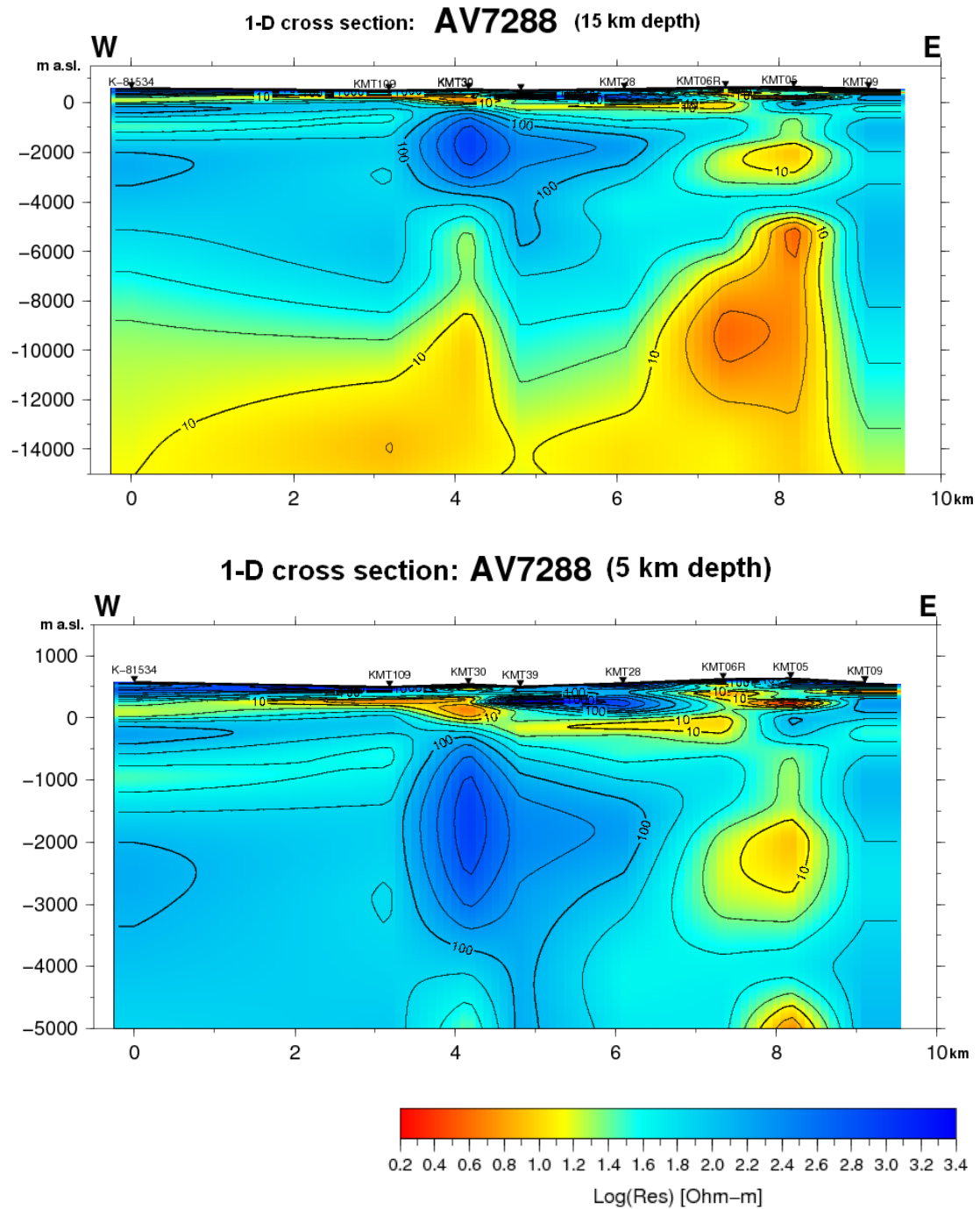


Figure 17. 1-D resistivity cross sections of MT soundings on profile AV7288, 15 km depth (Top) and 5 km depth (Bottom).

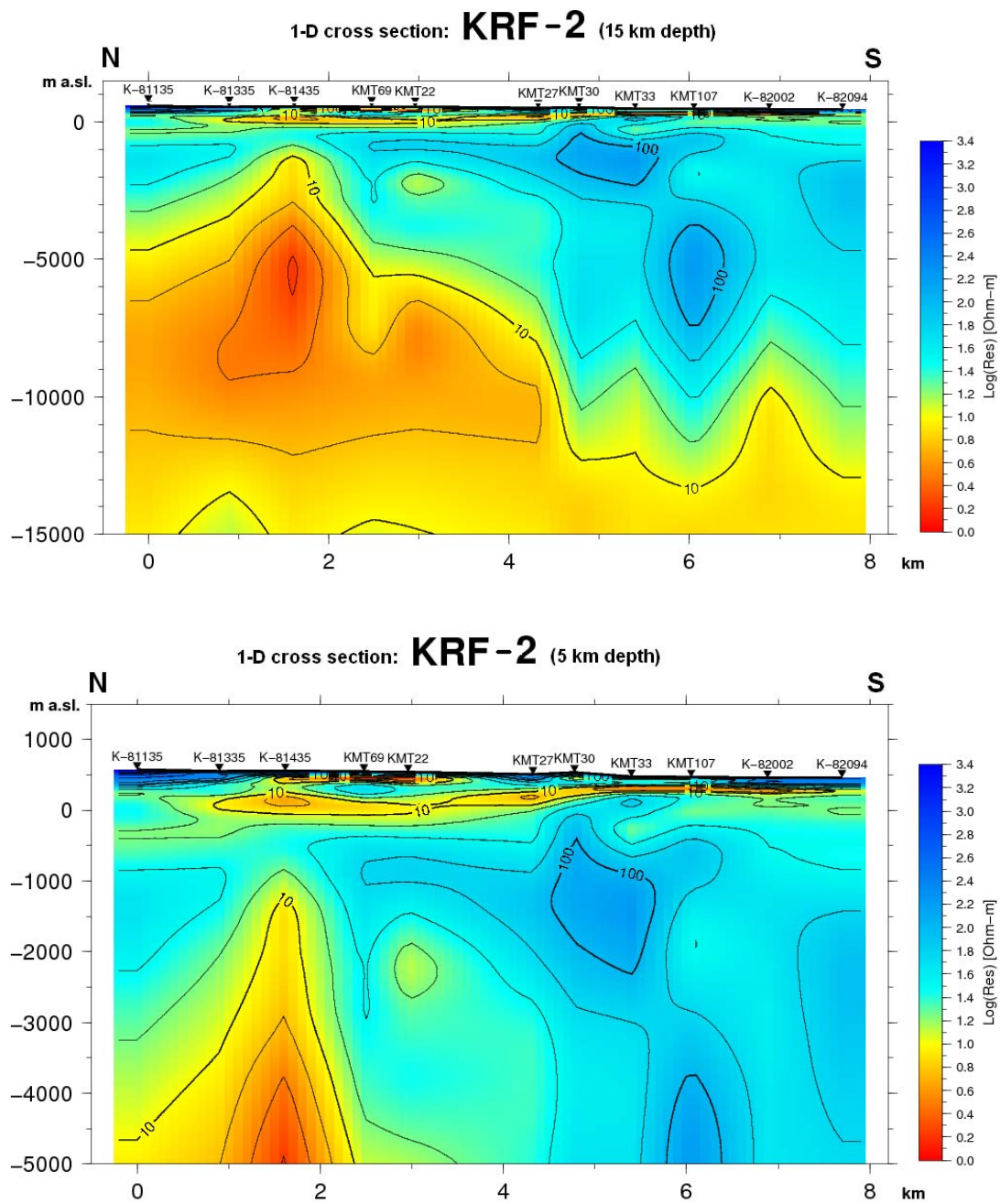


Figure 18. 1-D resistivity cross sections of MT soundings on profile KRF-2, 15 km depth (Top) and 5 km depth (Bottom).

6 2-D MT data inversion

6.1 The 2-D MT inversion

Like in general inversion processes, the forward modelling is very important in calculating the response and therefore it is used to calculate the misfit between the measured and calculated data. In an N-layered earth model we calculate the apparent resistivity and phase response of a given model using recursive formulas. On the other hand in 2-D MT forward modelling two diffusion equations are solved:

$$\nabla^2 E = i\omega\mu\sigma E \quad (6.1)$$

$$\nabla^2 H = i\omega\mu\sigma H \quad (6.2)$$

Both equations are second order Maxwell's equations (eq. 3.3).

In 2-D environment, the electric current flows parallel to the strike (Transfer Electric or TE mode), solved by equation (6.1). While for the electric current perpendicular to the strike (Transfer Magnetic or TM mode), solved by equation (6.2). The most common method in solving 2-D problem is the finite difference method (FD), in which the boundary conditions are defined in a given discrete element.

To perform 2-D inversion for both TE and TM mode (as well as TM-TE joint inversion) we used the 2-D inversion code REBOCC from Siripunvaraporn and Egbert (2000). In this program, we define the mesh grid as our elements to be solved by the equations and with boundary conditions. Figure 19A shows an example of the mesh grid design used in 2-D MT inversion. In the center of the mesh, we have the distance between grid planes as dense as possible and give increments on each side. There is no exact rule for the mesh grid design, but some practical guidelines can be found in the literature (see e.g. Simpson and Bahr, 2005). In Figure 19 the full model for TM mode is shown.

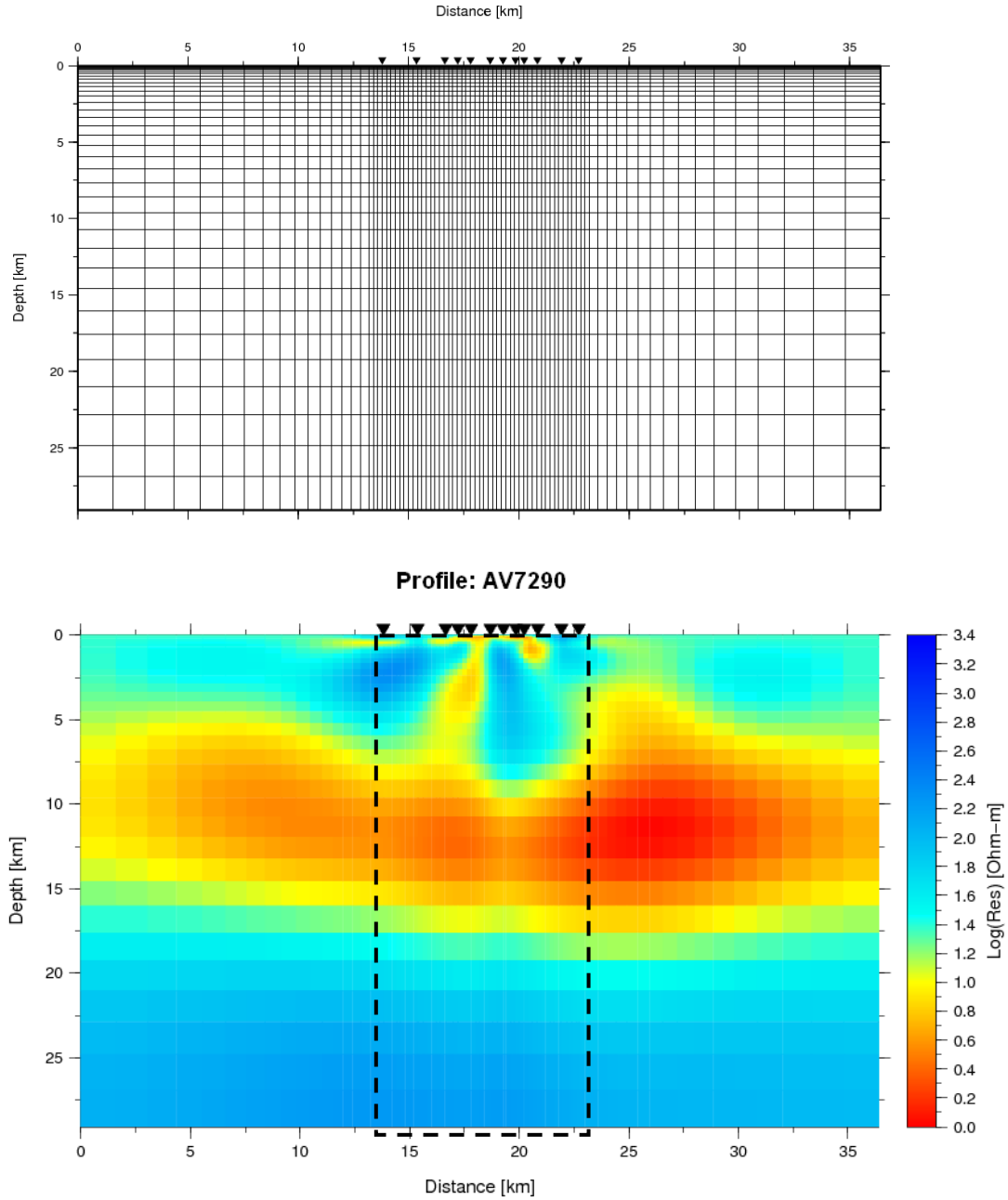


Figure 19. An example of a mesh grid design (Top). The length of the profile is approximately 9 km. On each side, the distance between the nodes is gradually increasing. The mesh grid reaches a distance just over 10 km to the east and west side of the profile (Bottom). The resistivity structure from the 2-D inversion using REBOCC for TM mode covering the whole mesh grid. The dashed lines represent the area covered by the MT data.

6.2 2-D resistivity model of Krafla

Two-dimensional MT resistivity models for two profiles (AV7290 and AV7288) perpendicular to the electrical strike direction as well as the regional geological strike direction (Figure 9) are obtained by separately inverting the TM and TE mode. In order to check the convergence of the inversion, a variety of 2-D inversions have been performed using different resistivities of a half-space as the initial model and different

error floor for apparent resistivity and phase. However, in all cases the results of the electrical resistivity structures show the same major features.

Using the half-space value of 2 Ωm for the initial model, the misfit of the measured data, especially for TM mode produced RMS values less than 3 for both profiles (Figures 22 and 23).

To avoid the artifact in the resulting model using REBOCC code, a large error floor (7%) for TE apparent resistivity data is chosen because of the high sensitivity of the TE mode to the 3-D structure. For the TE impedance phase and TM-mode data, an error floor of 4% is used. However, the large error floor might lead to over fitting of the data and produce fake structures. Therefore, the 7% error floor is chosen as the largest absolute value for the data. Consequently, the RMS error for TE and TM-TE joint inversion (which is influenced by the TE mode) remains high (7-10).

Figures 20 and 21 show the model result from 2-D inversion of the east-west profiles for different inversion processes: TM mode inversion (Figures 20A and 21A), TE mode inversion (Figures 20B and 21B) and TM-TE joint inversion (Figures 20C and 21C). The responses of the models are presented as pseudo-sections in Figures 22 and 23 where the calculated apparent resistivity and phase can be compared to the measured data. These pseudo-sections are calculated from TM and TE mode inverted separately. The response of the model from TM-TE joint inversion can be found in Appendix B. However, we will focus our analysis in TM mode.

In general the conductivity structure of the Krafla caldera contains two major conductors. A conductor at shallow depth appears as relatively thin high-conductivity layer with thickness varying along the profiles. The second conductor, at greater depth (8-18 km) can also be found at varying depths along the profiles.

For the uppermost 1-3 km, the models show the presence of a high-conductivity layer below a high resistivity surface layer. This conductor extends across the caldera. In AV7290, the thickest high-conductive layer appears below the Víti crater and the Leirhnjúkur hill which corresponds to highly altered zone presented on the surface as a cluster zone of surface manifestations. As for AV7288, the thickest shallow conductor appears in the central portion of the caldera.

The depth to the top of the shallow conductor is generally less than 500 m, it increases in the west portion and decreases in the east portion. It suggests that the thickness of the lava on the surface produced by the eruptions is mainly spilled out to the western portion of the caldera.

Shallow low resistivity layer in TM mode also appears in TE mode as the basic feature. It suggests that this feature is robust and required by both polarizations of the MT data. The fit of the data at very short periods in TE mode is generally fine for all sites (Figures 22 and 23).

The pseudo-sections of the measured data seem to be in good agreement with the pseudo-sections of the TM mode in Figures 22 and 23 except for the AV7290 impedance phase response. While for the TE mode, the good agreement is only valid for the very short periods.

The depth to the bottom of the deeper conductor is less certain since there is some misfit in the impedance phase of the TM data in AV7290. The only site that has the lowest phase in the measured data is K-81503 while the other sites are higher.

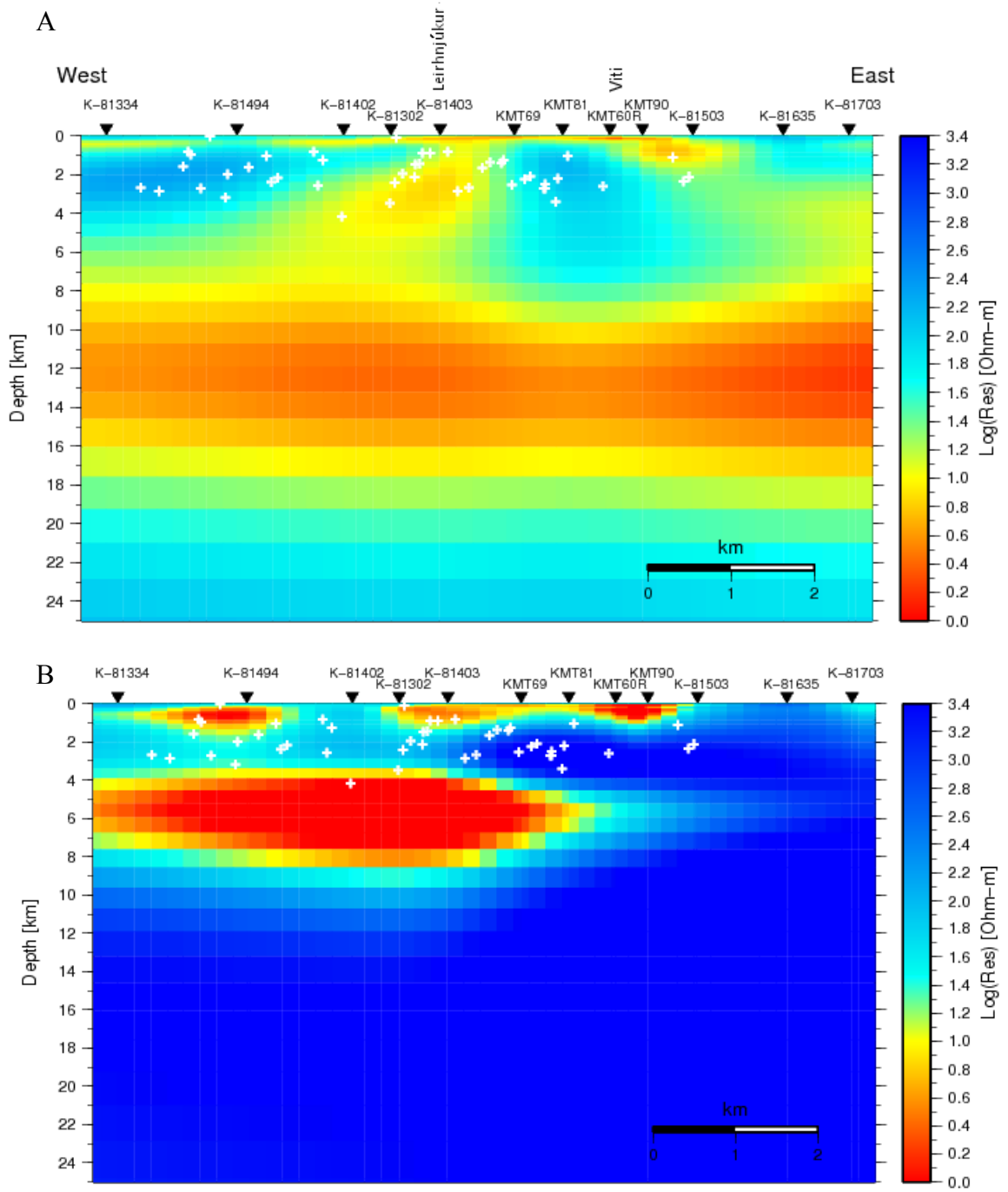


Figure 20. The 2-D inversion (REBOCC) models for AV7290. (A). TM mode inverted separately, overall RMS=2.20. (B) TE mode inverted separately, overall RMS=7.70. (C) TM-TE joint inversion, overall RMS=7.8. White crosses denote projected earthquakes, located at a distance less than 500 m away from the profile, recorded during the 1988 inflation event (Buck et al., 2006).

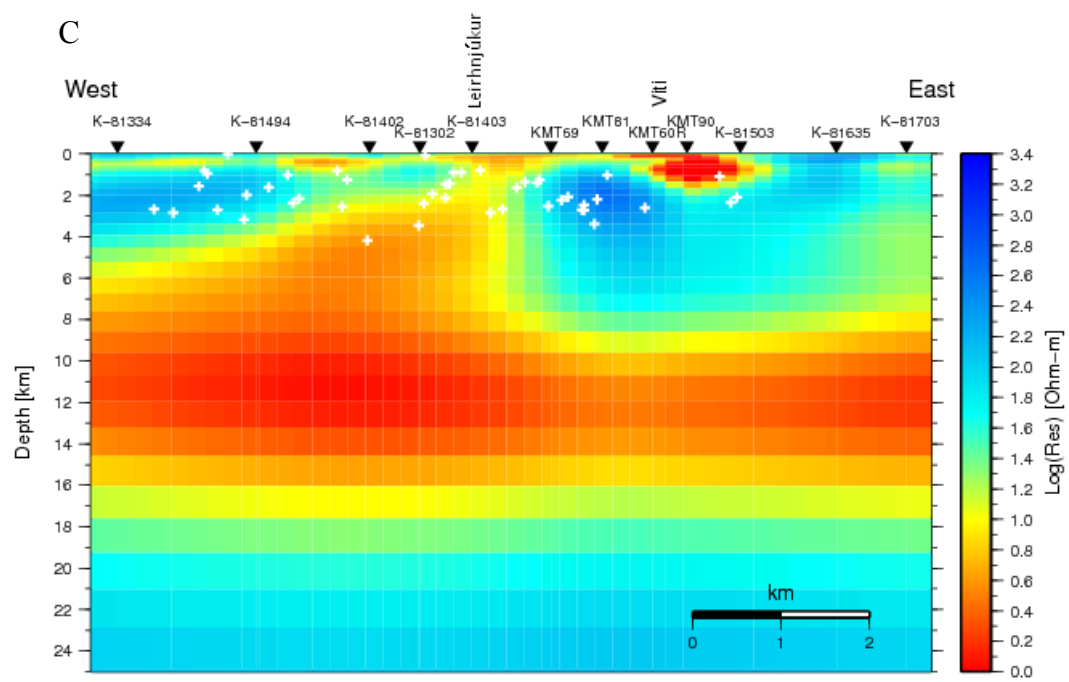


Figure 20. (continued)

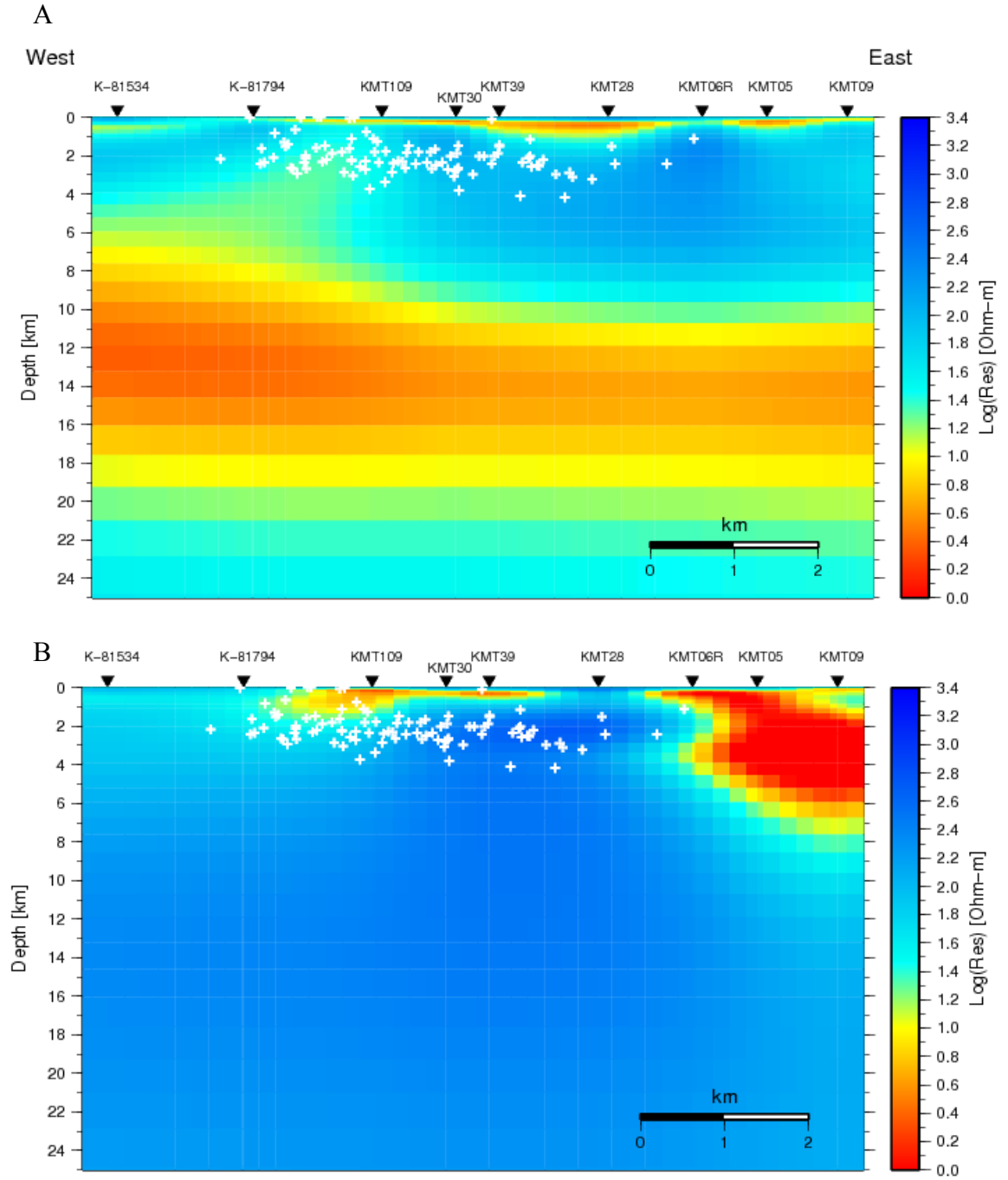


Figure 21. The 2-D inversion (REBOCC) model for AV7288. (A). TM mode inverted separately, overall RMS=1.82, (B) TE mode inverted separately, overall RMS=6.39. (C) TM-TE joint inversion, overall RMS=8.18. White crosses denote projected earthquakes, located at a distance less than 500 m away from the profile, recorded during 1988 inflation event (Buck et al., 2006).

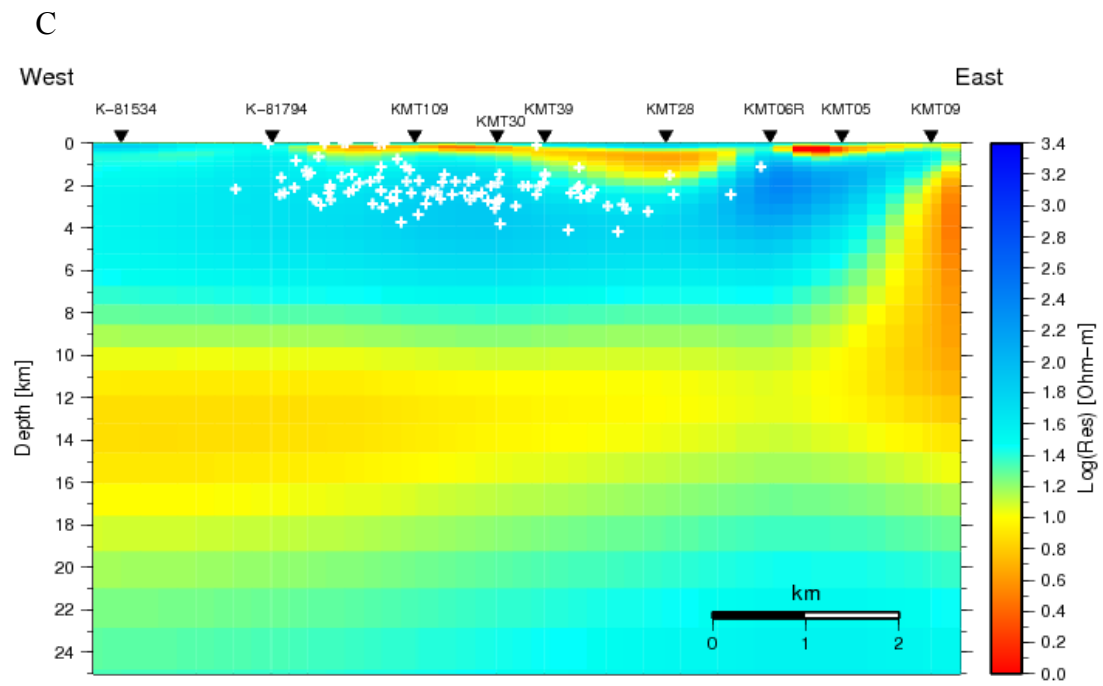


Figure 21. (continued)

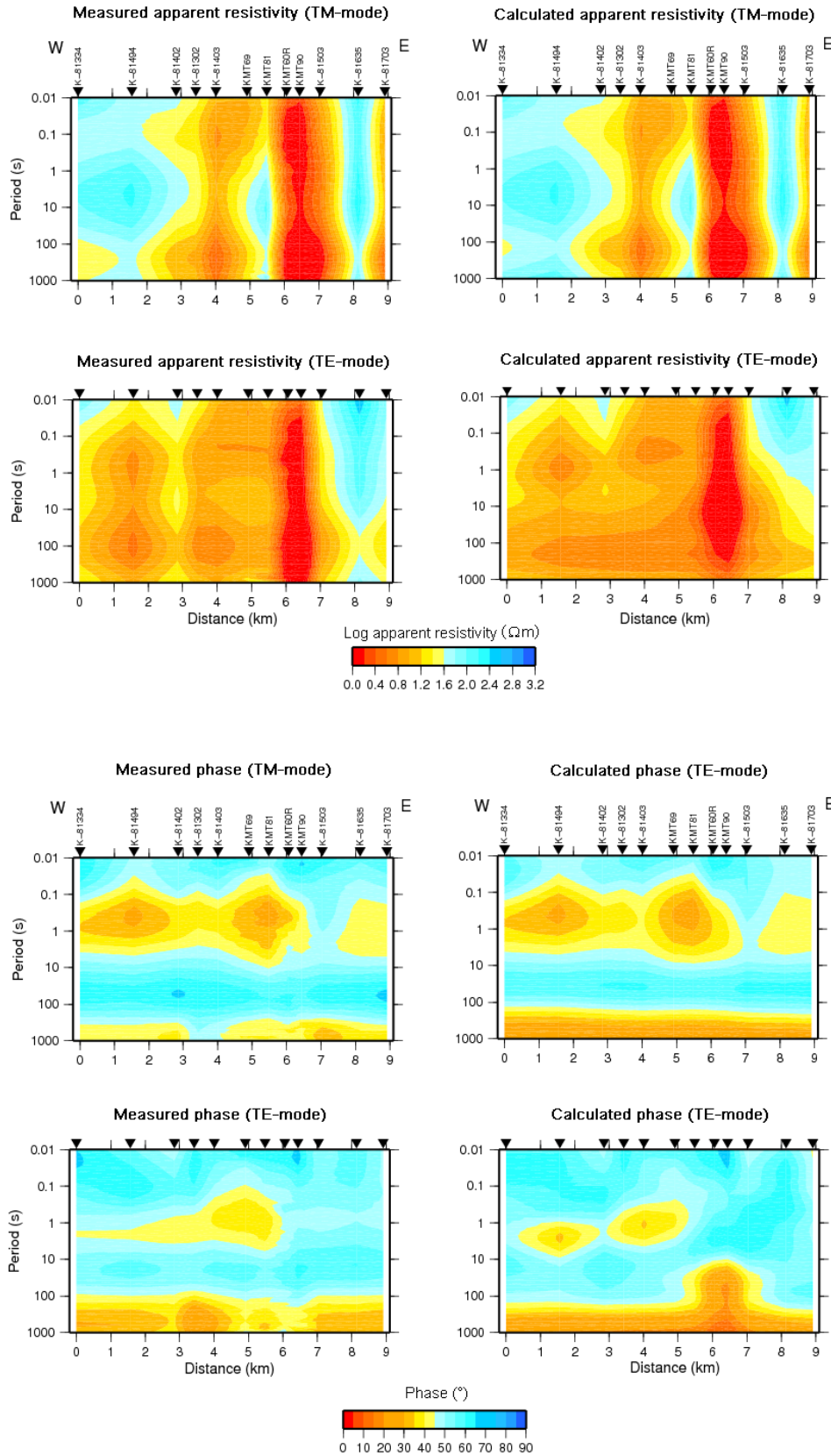


Figure 22. Measured (left) and calculated (right) apparent resistivity and phase pseudo-section from the model of the AV7290 profile in Figure 20. The MT data and the calculated responses of TM-TE joint inversion can be found in Appendix B.

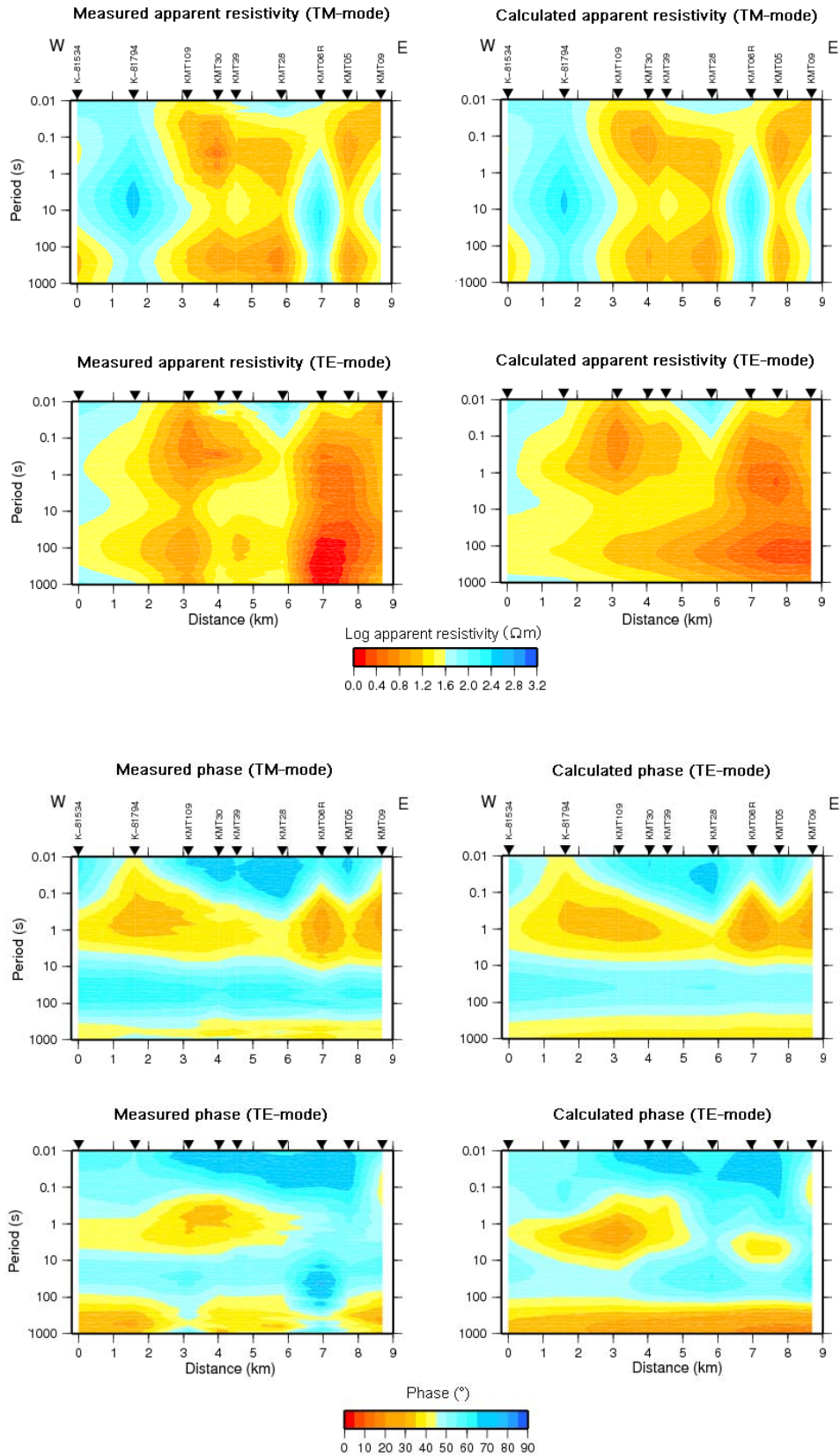


Figure 23. Measured (left) and calculated (right) apparent resistivity and phase pseudo-section from the model of the AV7288 profile in Figure 21. The MT data and the calculated responses of TM-TE joint inversion can be found in Appendix

7 Analysis and discussions

7.1 Structure of the upper 3 km

For the uppermost crust within the Krafla caldera, the 2-D resistivity model is mainly associated with hydrothermal alteration, fluid chemistry and change in porosity. While on the surface, eruption products which are composed of pillow lavas, pillow breccias and hyaloclastite tuffs are presented in our model as high resistive cover with thickness of less than several hundred meters.

At the uppermost 3 km, both the 1-D and 2-D models exhibit low-resistivity ($<10 \Omega\text{m}$) layers at less than 2 km depth which correspond to the rock alteration zone beneath the surface (Figures 24 and 25). Surface manifestations cluster between stations K-81302 and K-81503 in profile AV7290 correspond to the lowest resistivity values of this layer and present on the average a thicker layer as compared to the western part. In the western part, where there are no obvious geothermal manifestations on the surface but the relatively thin low-resistivity layer exists, suggests that a hydrothermal fluid circulation may exist below. In AV7288 (Figure 25) the thickest low resistivity layer at shallow depth appears below the surface manifestations cluster on the eastern part and also in the center part of the caldera where there are no obvious geothermal manifestations on the surface.

This shallow conductor represents the increase of clay associated with hydrothermal alteration and characterizes the impermeable clay cap in geothermal systems particularly in high-temperature geothermal fields in Iceland. The top of this layer is where the low hydrothermal alteration occurs (at temperature 50-100°C) and appears as the beginning of smectite-zeolite zone which is also marked by the increasing conductivity with the increasing depth. The conductivity reaches high values and starts to decrease with depth which correlates with the presence of the mixed-layer clay zone (230-250°C). Beneath this layer, the top of the high resistive core seems to correlate with a change in alteration mineralogy from smectites to mixed clays and chlorites and epidote (Árnason et al., 2000).

Beneath the low resistivity layer, the resistivity increases with increasing depth, the high resistive core. Within this seismically active zone the porosity is mainly controlled by the presence of fractures and therefore controls the resistivity values when it is filled by fluids. Below at a greater depth, there is a conductive structure at a depth of approximately 8 km, except below Leirhnjúkur, Site K-81403, where the deeper conductor reaches shallow depth.

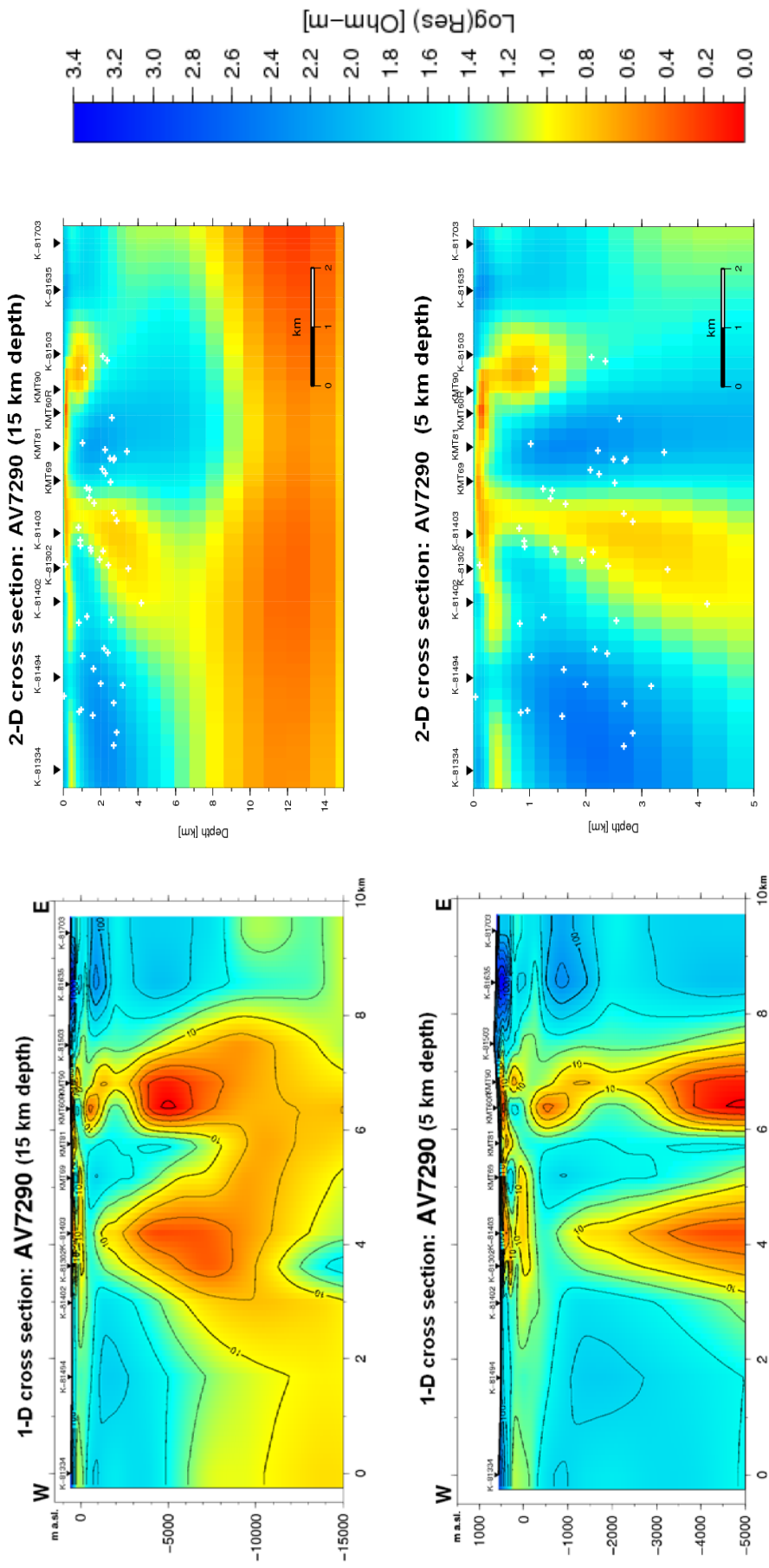


Figure 24. 2-D TM mode resistivity cross sections of 15 km and 5 km depths, respectively. Results are compared to 1-D results for profile AV7290. White crosses in the 2-D model represent the hypocenters of the earthquakes during the inflation period in 1988 (Buck et al., 2006).

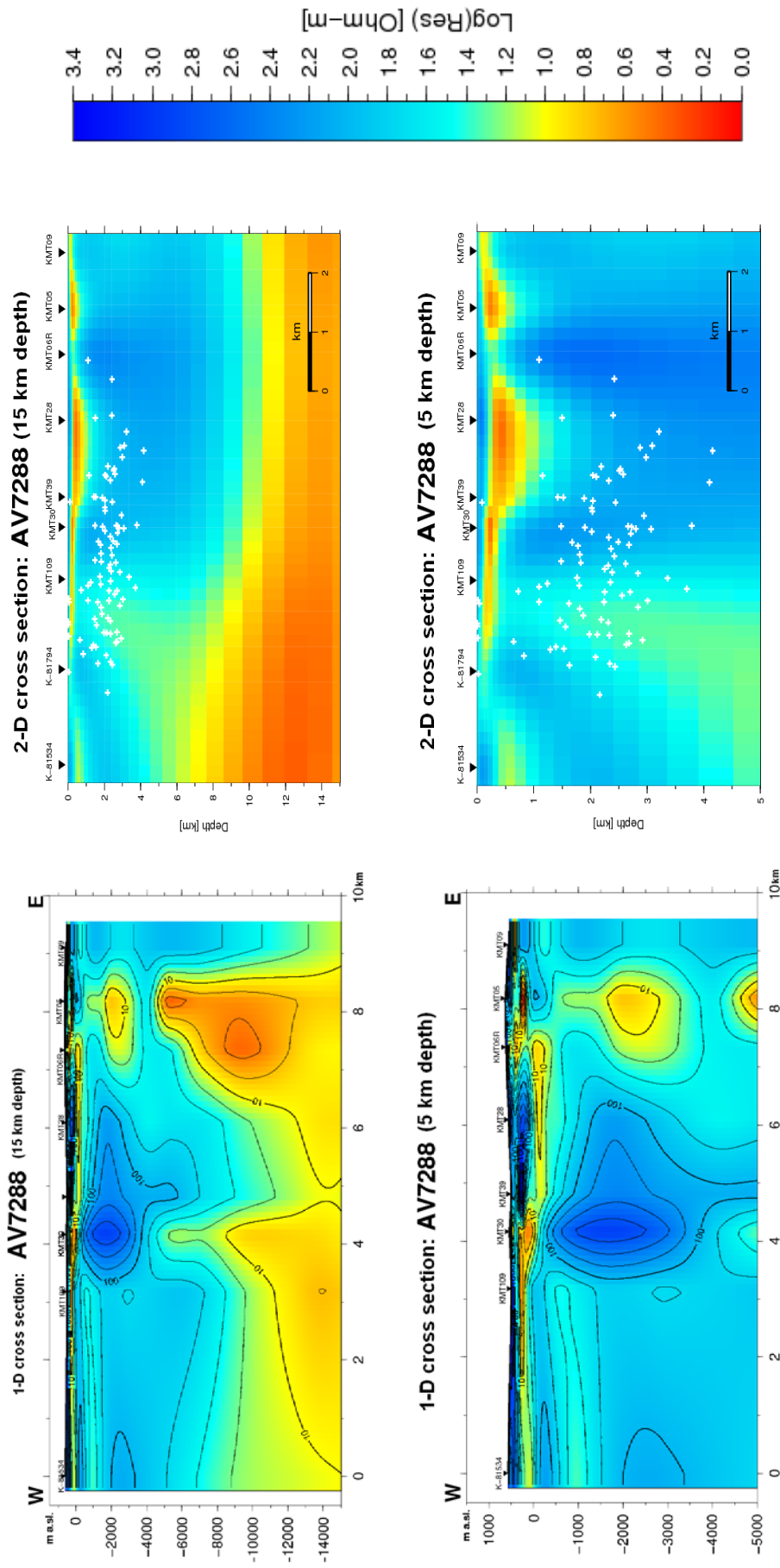


Figure 25. 2-D TM mode resistivity cross sections of 15 km and 5 km depths, respectively. Results are compared to 1-D results for profile AV7288. White crosses in the 2-D model represent the hypocenters of the earthquakes during the inflation period in 1988 (Buck et al., 2006).

7.2 Midcrustal and deeper structures

The two up-doming conductors in the 1-D model on profile AV7290 correlate fairly well with the S-wave shadows defined by Einarsson (1978). These anomalies are slightly different in the 2-D models (Figures 24 and 25). The eastern dome, resistivity approximately less than $15 \Omega\text{m}$ seems to be confined to a shallow depth within the SE tail of the eastern shear wave attenuation zone. If fed from below the upwelling stem of the eastern anomaly is not visible in our model. The conductive dome near Leirhnjúkur coincides with the inflation center of the shallow magma chamber merging with a deeper conductive layer at mid-crustal depths, below the seismogenic zone. Although the hypocentral depths are not well defined, there were fewer earthquakes during inflation periods that originate within the conductors than around them.

The conductive domes are most likely associated with interconnected melt and thus of great interest from a hydrothermal exploration standpoint. The temperature of the magma chamber should be higher than 1100°C (Jónasson, 1994) and the presence of the rhyolitic volcanism product around the caldera reflects the presence of rhyolitic magma near the magma chamber with lower temperatures due to cooling effect of the hydrothermal system with temperature interval $850^\circ\text{--}950^\circ\text{C}$ (Figure 26). However, there is no geothermal well to confirm the thermal gradient in the western part of the caldera.

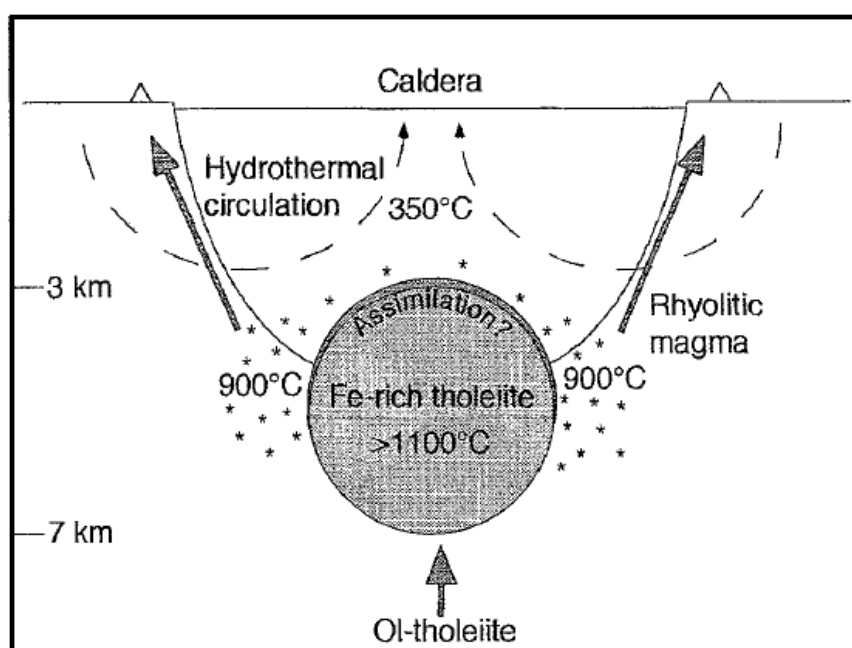


Figure 26. Simplified representation of thermal environment of the active magma chamber or intrusive domain during rhyolite genesis (Jónasson, 1994).

Earthquakes during the 1974-1980 and 1988 inflation periods are confined to the southern part of the caldera and they are more intense in the SW part than SE part. These earthquakes are most likely associated with crack opening adjacent to the magma accumulation zone. Both magmatic and hydrothermal fluids may be enhancing this process. More recent seismicity seems to be confined to active geothermal areas (Tang et al., 2005).

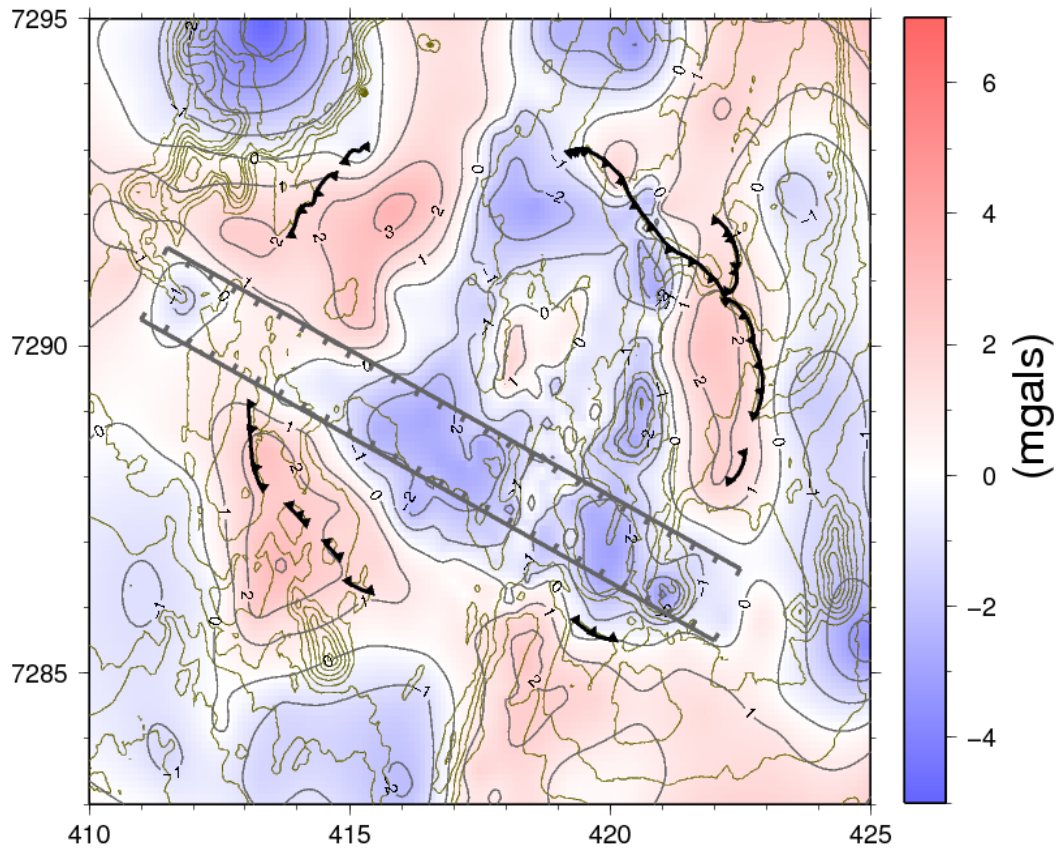


Figure 27. De-trended Bouguer gravity map (mgals) of the Krafla area (Árnason et al., 2009 modified from Johnsen, 1995). The caldera rim is denoted by hedge black lines, while the ESE-WNW transform graben inferred from the gravity data is denoted by the gray fault lines.

Figure 27 shows a de-trended Bouguer gravity map of the Krafla caldera and its surroundings. The Figure shows that there is a relative gravity low within the caldera. Superimposed on the gravity low is a gravity high at Leirhnjúkur which reflects the intrusions and the presence of a magma chamber (Árnason et al., 2009). This anomaly coincides with the 2-D MT cross section of TM mode in Figure 24.

A deep conductor at 10 km depth in MT models, can be found under most of Iceland (Björnsson et al., 2005). Figure 28 shows the depth to the deep conductor beneath Iceland. A profile across Krafla (Figure 28 bottom) indicates decreasing depth to top of the conductor towards the Krafla caldera.

This deep conductor was explained as partial melt somehow associated with the crust-mantle boundary (e.g. Beblo and Björnsson, 1978). Seismic velocity structure (Brandsdóttir et al., 1997) does not support the presence of the melting zone since there is no seismic wave attenuation. Another explanation of the conductive layer (Árnason et al., 2010) is that below the ductile-brittle boundary, magmatic water is trapped within the plastic rock (Fournier, 1999).

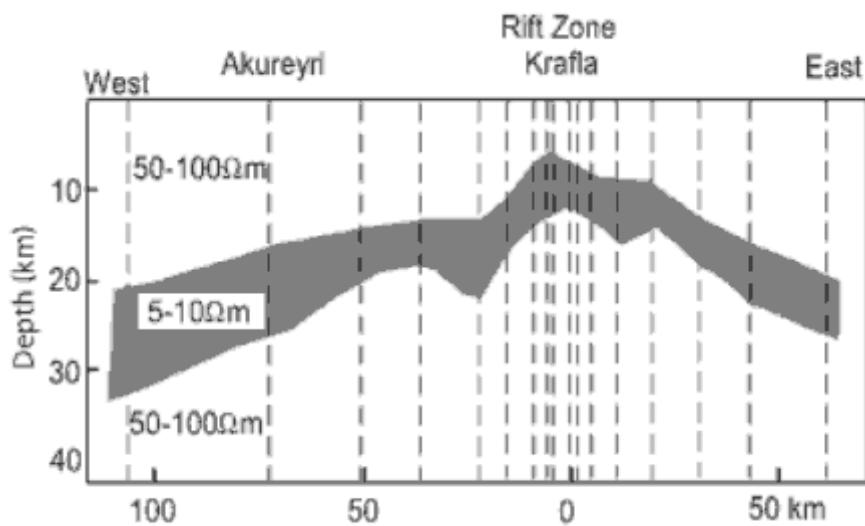
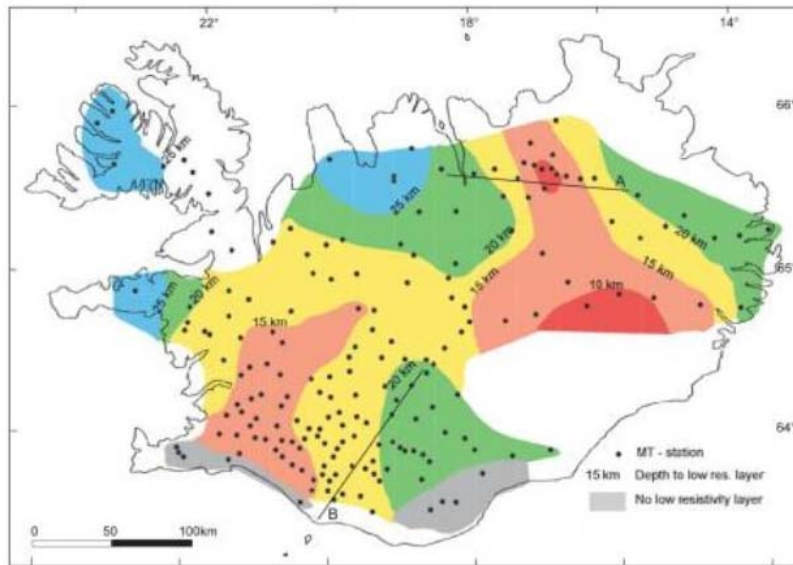


Figure 28. A map showing the depth to the deep conductor in the Icelandic crust (taken from Björnsson et al., 2005) (Top) and a 1-D MT profile crossing the Krafla volcanic system, location shown above (taken from Beblo et al., 1983) (Bottom).

The apparent connection between the deeper and the shallow conductor is poorly resolved due to the reduced skin depth in the overlying conductive material. In general, the 2-D cross sections (especially AV7290) are in a good agreement with previous geophysical and geodetic results as presented in Figure 29.

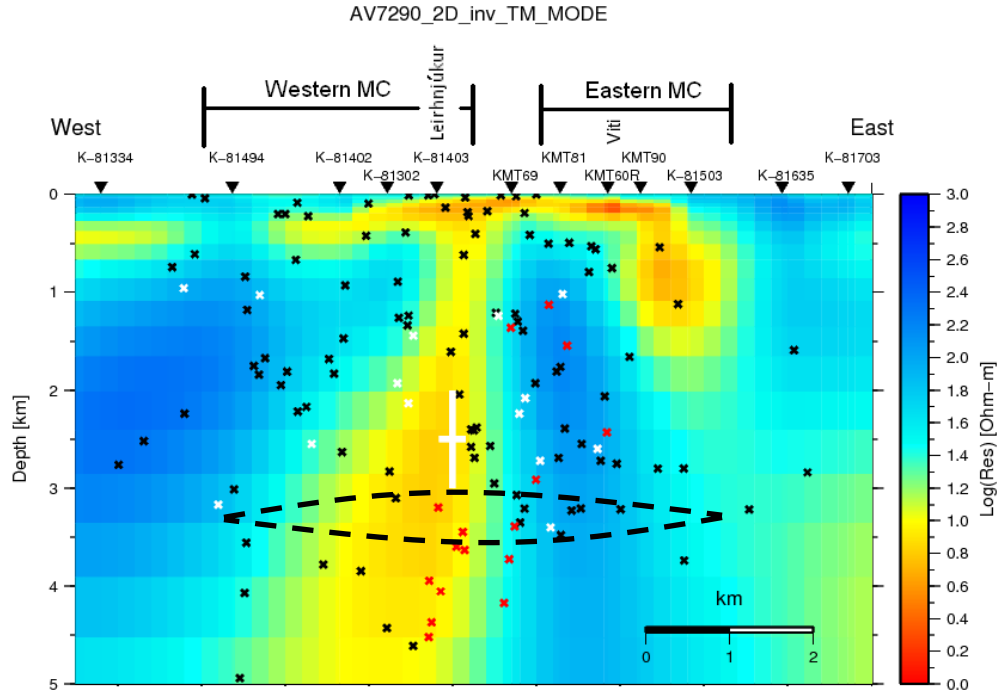


Figure 29. Comparison of the 2-D TM mode inversion result of profile AV7290 and several previous studies in the Krafla area. Earthquake hypocenters during the inflation periods 1974-1980 (black stars) and 1988 (white stars) and seismicity during 2009 (red stars) located by the IMO network are also presented (IMO database: <http://www.vedur.is/skjalfjar-og-eldgos/jardskjalftar>). Western and Eastern MC denote the S-wave shadow zones determined by Einarsson (1978) and the white bar in the middle of the low resistivity body denotes inflation and deflation centers as determined by Tryggvason (1999). Black dashed lines represent the approximation of the low seismic velocity zone (Brandsdóttir et al., 1997).

Figure 29 summarized the previous geophysical and geodetic studies within the Krafla caldera compared to 2-D TM mode resistivity model of AV7290. The magma chambers delineated from the S-wave shadows (Einarsson, 1978) are presented by the east and west magma chamber's boundary denote by Western MC and Eastern MC on top of the figure. The presence of conductive body at 1-5 km depth in 2-D MT resistivity model coincides with the western magma chamber (Western MC) boundaries, while a similar feature does not coincide with the eastern shear wave attenuation zone. Our profile lies at the northern boundary of the eastern S-wave attenuation zone which not well constrained by the seismic data (Einarsson 1978).

The most precise earthquake locations recorded during the inflation in 1988 at Krafla (Brandsdóttir, pers. Comm., Des. 2009) are presented in Figure 29 by the white stars. They are clustered on the each side of the conductive body indicating the highly stress zone as an effect of the inflation process and produces the high seismicity zone. Another earthquake hypocenters recorded in 2009 (denotes by red stars) also appears clustered in the eastern side of the conductive body and support the dimension of the magma chamber in the resulting model.

From seismic refraction studies (Brandsdóttir et al., 1997), a low velocity anomaly interpreted as a magma chamber sits at the top of the high-velocity dome with its top

at a depth of 3 km. It is a 2-6 km wide, 0.75-1.8 km thick lens of low velocities, with a velocity of 3 km/s. The top of this anomaly coincides with the top of the conductive dome but not with its lateral extent.

The top of the magma chamber in 2-D model of AV7290 seems to coincide with the boundary of the absence of the earthquakes below 3 km depth. The top of the deeper conductor, as can be found all over Iceland, appears in our model at 8 km depth. However, this approximative depth to the top of the deeper conductor in AV7290 seems to be less certain since the apparent resistivity and phase response to the model at long periods, especially in impedance phase, is in less agreement with the measured impedance phase.

Tilt and distance measurements of the inflation event in the Krafla caldera during 1975-1989 determined that the mean center of the inflation is located at 2 and 3 km depth near 65°N 42,883' and -16°W 47.983 (Tryggvason, 1999). This result also presented in Figure 29 by the white bars in the middle of the conductive body denoting the range of the inflation center in vertical (depth) and horizontal direction (distance).

7.3 Sensitivity test

For the western up-doming deep conductor that coincides with the western S-wave shadow, the lateral extent of the conductive body in the TM mode seems to be smaller than defined by the S-wave shadows, while the results of the TM-TE joint inversion show that the conductive body appears farther to the west (Figure 20C). Here we performed a sensitivity test to assess the sensitivity of the data to the presence of this conductive body. The sensitivity has been tested by the TM mode data of site K-81494 as presented in Figure 20. First by removing the conductive body from the TM model and later replacing the conductive body in the TM model by the extended body as presented in TM-TE result. This sensitivity test was performed using forward modelling.

By removing the conductive body from the model, the TM mode response of the model shown the complete cancelation of the anomaly at longer period as presented by the red lines in Figure 30. This first test suggests that the conductive body should exist in the model. The conductive body is then replaced by the body with extension to the west as in TM-TE joint inversion model (Figure 20C). The result in Figure 30 shows the response to the model (green lines). However, the presence of this conductive body which we interpreted as a magma chamber is not laterally extended to the west, but instead it has some dipping angle to the west and somehow connected to the deeper conductor.

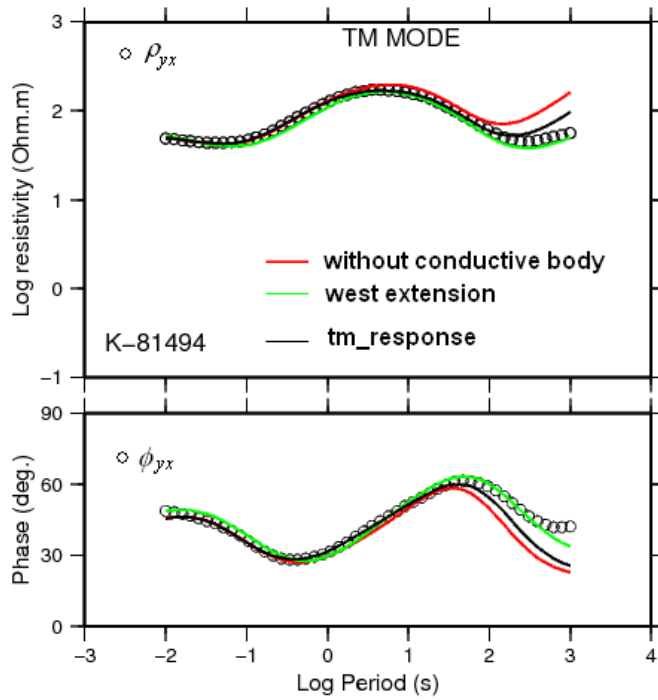


Figure 30. Apparent resistivity and impedance phase sounding curves of the TM mode at site K-81494 in the western part of profile AV7290. Green solid lines are the model response of extended magma chamber to the west as shown in Figure 12C. Red lines are the model response when the magma chamber is removed from the model. Black curves are the TM mode response of our best-fit.

8 Conclusions

A significantly improved image of the conductivity structure beneath the Krafla central volcano has been constructed using 2-D inverse modeling of magnetotelluric data and correlation with local seismic data.

The uppermost conductive structure which correlates with hydrothermal activities is well resolved. As the depth increases, the electrical complexity is also increasing and affecting the MT data. In the midcrustal region, rocks below 2 km depth with resistivity reaching 1000 Ωm is interpreted to have a little alteration and has porosities under one percent as a resistive core.

Magma chamber delineated from the profile AV7290 on the western part of the caldera is also well resolved with plausible dimension as proposed by the sensitivity test. While on the eastern part, low resistivity anomaly (between 10-20 Ωm) was found with no correlation to any other anomaly presented by other studies. Since our profile crosses the proximity of the northern boundary of eastern magma chamber, we suggest that this boundary to be located southern of our profiles.

Wide range of periods in the MT data allows us to investigate the deeper structure of the caldera and exhibit the deeper conductor. The thickness of this layer is not well constrained since the fit of the impedance phase at longest periods for most of sites in AV7290 are poor. Nonetheless, in AV7288, the calculated phase at longest periods have a very small misfit.

Two-dimensional analyses of MT data and interpretation in Krafla have revealed its strength and limitation. The TM mode data has provided a geologically reasonable image especially in the uppermost few kilometers. Before the TE mode anomaly can be simulated through 3-D modelling, fewer structures were delineated using 2-D analyses with high confidence. In addition, the analysis provided by the impedance phase tensor analysis should be performed to get a clearer pictures of the complexity of the electrical structures of the area.

References

- Árnadóttir, T., Sigmundsson, F., Delaney, P. T., 1998. Sources of crustal deformation associated with the Krafla, Iceland, eruption of September 1984, *Geophys. Res. Lett.*, 25(7), 1043–1046.
- Árnason, K., 1989. Central loop transient electromagnetic sounding over a horizontally layered earth. Orkustofnun, Reykjavik, report OS-89032/JHD-06, 129 pp.
- Árnason, K., Karlsdóttir, R., Eysteinnsson, H., Flóvenz, Ó. G., Guðlaugsson, S. Th., 2000. The resistivity structure of high-temperature geothermal systems in Iceland. Proceedings of the WGC 2000, Japan, 923-928.
- Árnason, K., 2006. TEMTD, a program for 1D inversion of central-loop TEM and MT data. Short manual. Unpublished ÍSOR internal report, Reykjavik, Iceland, 17 pp.
- Árnason, K., Vihjálmsen, A. M., Björnsdóttir, Th., 2009. A study of the Krafla volcano using gravity, micro-earthquake and MT data. Iceland GeoSurvey report ÍSOR-2009/067, Reykjavik, Iceland 67 pp, manuscript.
- Árnason, K., Eysteinnsson, H., Hersir, G. P., 2010. Joint 1D inversion of TEM and MT data and 3D inversion of MT data in the Hengill area SW Iceland. *Geothermics*, in press.
- Beblo, M., Björnsson, A., 1978. Magnetotelluric investigation of the lower crust and upper mantle beneath Iceland. *J. Geophys.*, 45, 1-16.
- Beblo, M., Björnsson, A., 1980. A model of electrical resistivity beneath NE-Iceland, correlation with temperature. *J. Geophys.*, 47, 184-190.
- Beblo, M., Björnsson, A., Árnason, K., Stein, B., Wolfgram, P., 1983. Electrical conductivity beneath Iceland – constraints imposed by magnetotelluric results on temperature, partial melt, crust- and mantle structure. *J. Geophys.*, 53, 16-23.
- Björnsson, A., Sæmundsson, K., Einarsson, P., Tryggvason, E., Grönvold, K., 1977. Current rifting episode in north Iceland. *Nature*, 266, 318–323.
- Björnsson, A., 1985. Dynamics of Crustal Rifting in NE Iceland. *J. Geophys. Res.*, 90, 151-162.
- Björnsson A., Eysteinnsson H., Beblo, M., 2005. Crustal formation and magma genesis beneath Iceland: Magnetotelluric constraints. *Plates, Plumes and Paradigms*, Geological Society of America, Special Paper 388, 665-686.
- Brandsdóttir, B., Menke, W., Einarsson, P., White, R. S., Staples, R. K., 1997. Faroe-Iceland ridge experiment, 2. Crustal structure of the Krafla central volcano. *J. Geophys. Res.*, 102, 7867-7886.
- Brandsdóttir, B., Menke, W., 1992. Thin low-velocity zone within the Krafla caldera, ne-Iceland attributed to a small magma chamber. *Geophys. Res. Lett.*, 24, 2381-2384.
- Brandsdóttir, B., Menke, W., 2008. The seismic structure of Iceland. *Jökull*, 58, 17–34.

- Buck, W. R., Einarsson, P., Brandsdóttir, B., 2006. Tectonic stress and magma chamber size as controls on dike propagation: Constraints from the 1975-1984 Krafla rifting episode. *J. Geophys. Res.*, 111, doi:10.1029/2005JB003879, B12404, 15 pp.
- Cagniard, L., 1953. Basic Theory of the magnetotelluric method of geophysical prospecting. *Geophysics*, 18, 605-635.
- Caldwell, T. G., Bibby, H. M., Brown, C., 2004. The magnetotelluric phase tensor. *Geophys. J. Int.*, 158, 457-469.
- Constable, S. C., Parker, R. L., Constable, C. G., 1987. Occam's inversion: A practical algorithm for generating smooth models from electromagnetic sounding data. *Geophysics*, 52, 289-300.
- Darbyshire, F. A., White, R. S., Priestley, K. F., 2000. Structure of the crust and uppermost mantle of Iceland from a combined seismic and gravity study. *Earth and Planetary Science Letters*, 181, 409-428.
- de Zeeuw-van Dalfsen, E., Pedersen, R., Sigmundsson, F., Pagli, C., 2004. Satellite radar interferometry 1993–1999 suggests deep accumulation of magma near the crust-mantle boundary at the Krafla volcanic system, Iceland, *Geophys. Res. Lett.*, 31, L13611, doi:10.1029/2004GL020059.
- de Zeeuw-van Dalfsen, E., Rymer, H., Williams-Jones, G., Sturkell, E., Sigmundsson, F., 2006. Integration of micro-gravity and geodetic data to constrain shallow system mass changes at Krafla Volcano, N Iceland. *Bull. Volcanol.*, 68, 420-431.
- Einarsson, P., 1978. S-wave shadows in the Krafla caldera in NE-Iceland, evidence for a magma chamber in the crust. *Bull. Volcanol.*, 41, 187-195.
- Einarsson, P., Sæmundsson, K., 1987. Earthquake epicenters 1982-1985 and volcanic systems in Iceland. A map in: Þ. I. Sigfússon ed. *Í hlutarins eðli*, Festschrift for Þorbjörn Sigurgeirsson, Menningarsjóður, Reykjavík.
- Einarsson, P., 1991. Earthquakes and present-day tectonics in Iceland. *Tectonophysics* 189, 261-279.
- Einarsson, P., 2008. Plate boundaries, rift and transforms in Iceland. *Jökull*, 58, 35-58.
- Fournier, R. O., 1999. Hydrothermal processes related to movement of fluid from plastic into brittle rock in the magmatic-epithermal environment. *Economic Geology*, 94, 8, 1193-1211.
- Gamble, T. D., Goubau, W. M., Clarke, J., 1979a. Magnetotellurics with a remote magnetic reference. *Geophysics*, 44, 53-68.
- Gamble, T. D., Goubau, W. M., Clarke, J., 1979b. Error analysis for remote reference magnetotellurics. *Geophysics*, 44, 959-968.
- Hersir, G. P., Björnsson, A., 1991. Geophysical exploration for geothermal resources. Principles and applications. UNU-GTP, Iceland, report 15, 94 pp.
- Hill, G. J., Caldwell, T. G., Heise, W., Chertkoff, D. G., Bibby, H. M., Burgess, M. K., Cull, J. P., Cas, R. A. F., 2009. Distribution of melt beneath Mount St Helens and Mount Adams inferred from magnetotelluric data. *Nature Geoscience*.
- Ichiki, M., Mishina, M., Goto, T., Oshiman, N., Sumitomo, N., Utada, H., 1999. Magnetotelluric investigations for the seismically active area in Northern Miyagi Prefecture, northeast Japan. *Earth Planet Space*, 51, 351-361.

- Ingham, M., 2005. Deep electrical structure of the Central Volcanic Region and Taupo Volcanic Zone, New Zealand. *Earth Planets Space*, 57, 591-603.
- Jiracek, G. R., Haak, V., Olsen, K. H., 1995. Practical magnetotelluric in a continental rift environment; in K.H. Olsen, ed., *Continental rifts: evolution, structure and tectonics*: New York, Elsevier, 103-129.
- Johnsen, G. V., 1995. Gravity map of the Krafla-area. In: EYJAR Í ELDHAFI. Björn Hróarsson, Dagur Jónsson and Sigurður Sveinn Jónsson (Eds.). *Gott mál*, 93-100. (In Icelandic).
- Jónasson, K., 1994. Rhyolite volcanism in the Krafla central volcano, north-east Iceland. *Bull. Volcanol.*, 56, 516-528.
- Jones, A. G., 1987. MT and reflection: An essential combination. *Geophys. J. R. Astr. Soc.*, 89, 7-18.
- Ledo, J., Queralt, P., Anna, M., Jones, A. G., 2002. Two-dimensional interpretation of three-dimensional magnetotelluric data: an example of limitations and resolution. *Geophys. J. Int.*, 150, 127-139.
- Mortensen, A. K. (editor), Guðmundsson, Á., Sigmundsson, F., Axelsson, G., Ármannsson, H., Björnsson, H., Ágústsson, K., Sæmundsson, K., Ólafsson, M., Karlsdóttir, R., Halldórsdóttir, S., Hauksson, T., 2009. Krafla geothermal system. A compilation of explorations and developments of the geothermal system and reevaluation of the conceptual model. Landsvirkjun report, LV-1009/111 and ÍSOR report, ÍSOR-2009/057 (In Icelandic), manuscript.
- Oskooi, B., Pedersen, L. B., Smirnov, M., Árnason, K., Eysteinnsson, H., Manzella, A., the GDO working group, 2005. The deep geothermal structure of the Mid-Atlantic Ridge deduced from MT data in SW Iceland. *Physics of the Earth and Planetary Interiors*, 150, 183-195.
- Pous, J., Heise, W., Schnegg, P., Muñoz, G., Martí, J., Soriano C., 2002. Magnetotelluric study of the Las Cañadas caldera (Tenerife, Canary Islands): structural and hydrology implications. *Earth and Planetary Science Letters*, 204, 249-263.
- Roy, K. K., Dey, S., Srivastava, S., Biswas, S., 2004. What to trust in a magnetotelluric model?. *J. Ind. Geophys. Union*, 8, 2, 157-171.
- Sigmundsson F., Vadon, H., Massonnet, D., 1997. Readjustment of the Krafla spreading segment to crustal rifting measured by satellite radar interferometry, *Geophys. Res. Lett.*, 24, 1843-1846.
- Simpson, F., Bahr, K., 2005. *Practical magnetotellurics*. Cambridge University Press. 254 pp.
- Siripunvaraporn, W., Egbert, G., 2000. An efficient data-subspace inversion method for 2-D magnetotelluric data. *Geophysics*, 65, 3, 791-803.
- Stenberg, B. K., Washburne, J. C., Pellerin, L., 1988. Correction for the static shift in magnetotellurics using transient electromagnetic soundings. *Geophysics*, 53, 11, 1459-1468.
- Sturkell, E., Einarsson, P., Sigmundsson, F., Geirsson, H., Ólafsson, H., Pedersen, R., de Zeeuw-van Dalssen, E., Linde, A. L., Sacks, I. S., Stefansson, R., 2006. Volcano geodesy and magma dynamics in Iceland, *J. Volc. Geotherm. Res.*, 150, 14-34.
- Sturkell, E., Sigmundsson, F., Geirsson, H., Ólafsson, H., Theodórsson, T., 2008. Multiple volcano deformation sources in a post-rifting period 1989-2005 behaviour of

- Krafla, Iceland constrained by leveling, tilt and GPS observations. *J. Volcanol. Geotherm. Res.*, 177, 405-417.
- Sæmundsson, K., 1978. Fissure swarms and central volcanoes of the neovolcanic zones of Iceland. *Geol. J. Special Issue*, 10, 415-432.
- Sæmundsson, K., 1991. Geology of the Krafla area. In: A. Gardarsson and Á. Einarsson, eds. *Náttúra Mývatns*, (The Nature of lake Mývatn), Icelandic Nature Sci. Soc., Reykjavík, 24-95.
- Swift, C. M., 1967. A magnetotelluric investigation of electrical conductivity anomaly in the southern United State. PhD Thesis. Massachusetts Institute of Technology, Cambridge, MA.
- Tang, C., Rial, J. A., Lees, J. M., 2005, Shear-wave splitting: A diagnostic tool to monitor fluid pressure in geothermal fields. *Geophys. Res. Lett.*, 32, L21317.
- Tikhonov, A. N., 1950. An investigation of electrical characteristics of deep strata of earth's crust. *Doklady, USSR*, 73, 2, 295-297.
- Tryggvason, E., 1986. Multiple magma reservoirs in a rift-zone volcano— Ground deformation and magma transport during the September 1984 eruption of Krafla, Iceland. *J. Volcanol. Geotherm. Res.*, 28, 1 – 44.
- Tryggvason, E., 1994. Surface deformation at the Krafla volcano, north Iceland, 1982– 1992, *Bull. Volcanol.*, 56, 98– 107.
- Tryggvason, E., 1995. Optical levelling tilt stations in the vicinity of Krafla and the Krafla fissure swarm. Observations 1976 to 1994. NVI Research Report 9505.
- Tryggvason, E., 1999. The Krafla center of inflations and deflations during the years 1975 to 1997. NVI Research Report 9901.
- Vozoff, K., 1986. Magnetotelluric method. Geophysics reprint series No.5, SEG.
- Vozoff, K., 1991. The magnetotelluric method: Chapter 8 in *Electromagnetic methods in applied geophysics*, Nabighian, M.N., ed. Investigations in geophysics n.3, v. 2 Applications part A and part B, Society of Exploration Geophysicists, Tulsa Oklahoma, 641-711.
- Wannamaker, P. E., Jiracek, G. R., Stodt, J. A., Caldwell, T. G., Gonzalez, V. M., McKnight, J. D., Porter, A. D., 2002. Fluid generation and pathways beneath an active compressional orogen, the New Zealand Southern Alps, inferred from magnetotelluric data, *J. Geophys. Res.*, 107(B6), 2117, doi:10.1029/2001JB000186.
- Wannamaker, P. E., Hasterok, D. P., Johnston, J. M., Stodt, J. A., Hall, D. B., Sodergren, T. L., Pellerin, L., Maris, V., Doerner, W. M., Groenewold, K. A., Unsworth, M. J., 2008. Lithospheric dismemberment and magmatic processes of the Great Basin–Colorado Plateau transition, Utah, implied from magnetotellurics, *Geochem. Geophys. Geosyst.*, 9, Q05019, doi:10.1029/2007GC001886.

Appendix A: From Maxwell's equations to the diffusion equations

The following explanations are mainly taken from Simpson and Bahr (2005).

The four Maxwell's equations below represent the behavior of the electromagnetic field at any frequency:

$$\nabla \times \mathbf{E} = -\frac{\partial \mathbf{B}}{\partial t}, \quad (3.1a)$$

$$\nabla \times \mathbf{H} = \mathbf{J} + \frac{\partial \mathbf{D}}{\partial t}, \quad (3.1b)$$

$$\nabla \cdot \mathbf{B} = 0, \quad (3.1c)$$

$$\nabla \cdot \mathbf{D} = \eta_f, \quad (3.1d)$$

where \mathbf{H} is the magnetic intensity (in A/m), \mathbf{J} is the electric current density (in A/m^2), \mathbf{D} is the electric displacement (in C/m^2), \mathbf{E} is electric field intensity (in V/m), \mathbf{B} is the magnetic induction (in T), and η_f is the electric charge density (in C/m^3).

Equation 3.1a is Faraday's Law, which states that time variations in the magnetic field induce corresponding fluctuations in the electric field flowing in a closed loop with its axis oriented in the direction of the induced field. Equation 3.1b is Ampere's Law, which states that any closed loop of electrical current will have an associated magnetic field of magnitude proportional to the total current flow. Equation 3.1c states that no free charges exist.

The constitutive relations for a homogeneous linear isotropic medium are given by:

$$\mathbf{B} = \mu \mathbf{H}, \mathbf{D} = \epsilon \mathbf{E} \text{ and } \mathbf{J} = \sigma \mathbf{E} \quad (A1)$$

where μ is the magnetic permeability of medium (H/m), ϵ is the electric permittivity (F/m) and σ is the conductivity (S/m).

Applying equations A1, Maxwell's equations can be written as:

$$\nabla \times \mathbf{E} = -\frac{\partial \mathbf{B}}{\partial t} \quad (A2a)$$

$$\nabla \times \mathbf{B} = \mu \sigma \mathbf{E} + \epsilon \mu \frac{\partial \mathbf{B}}{\partial t} \quad (A2b)$$

$$\nabla \cdot \mathbf{B} = 0 \quad (A2c)$$

$$\nabla \cdot \mathbf{E} = \eta_f / \epsilon \quad (A2d)$$

Assuming that no current sources exist within the Earth,

$$\nabla \cdot \mathbf{J} = \nabla \cdot (\sigma \mathbf{E}) = 0 \quad (A3)$$

For the case of an homogenous half-space (i.e. $\nabla \sigma = 0$):

$$\nabla \cdot (\sigma \mathbf{E}) = \sigma \nabla \cdot \mathbf{E} + \mathbf{E} \nabla \sigma = \sigma \nabla \cdot \mathbf{E} = 0 \quad (A4)$$

For the case of the Earth, a time-varying external magnetic field induces an electric field (according to Faraday's Law), which in turn induces a secondary, internal magnetic field (according to Ampere's Law). By taking the curl ($\nabla \times$) of equation A2a or A2b, we can derive a diffusion equation in terms of the time-varying electric field, from which information concerning the conductivity structure of the Earth can be extracted. For this purpose we make use of the vector identity:

$$\nabla \times (\nabla \times \mathbf{A}) = (\nabla \cdot \nabla \cdot \mathbf{A}) - \nabla^2 \mathbf{A} \quad (\text{A5})$$

where \mathbf{A} is any vector.

Taking curl of equation A2a, applying equation A1 and A4 (no current sources exist), we will get:

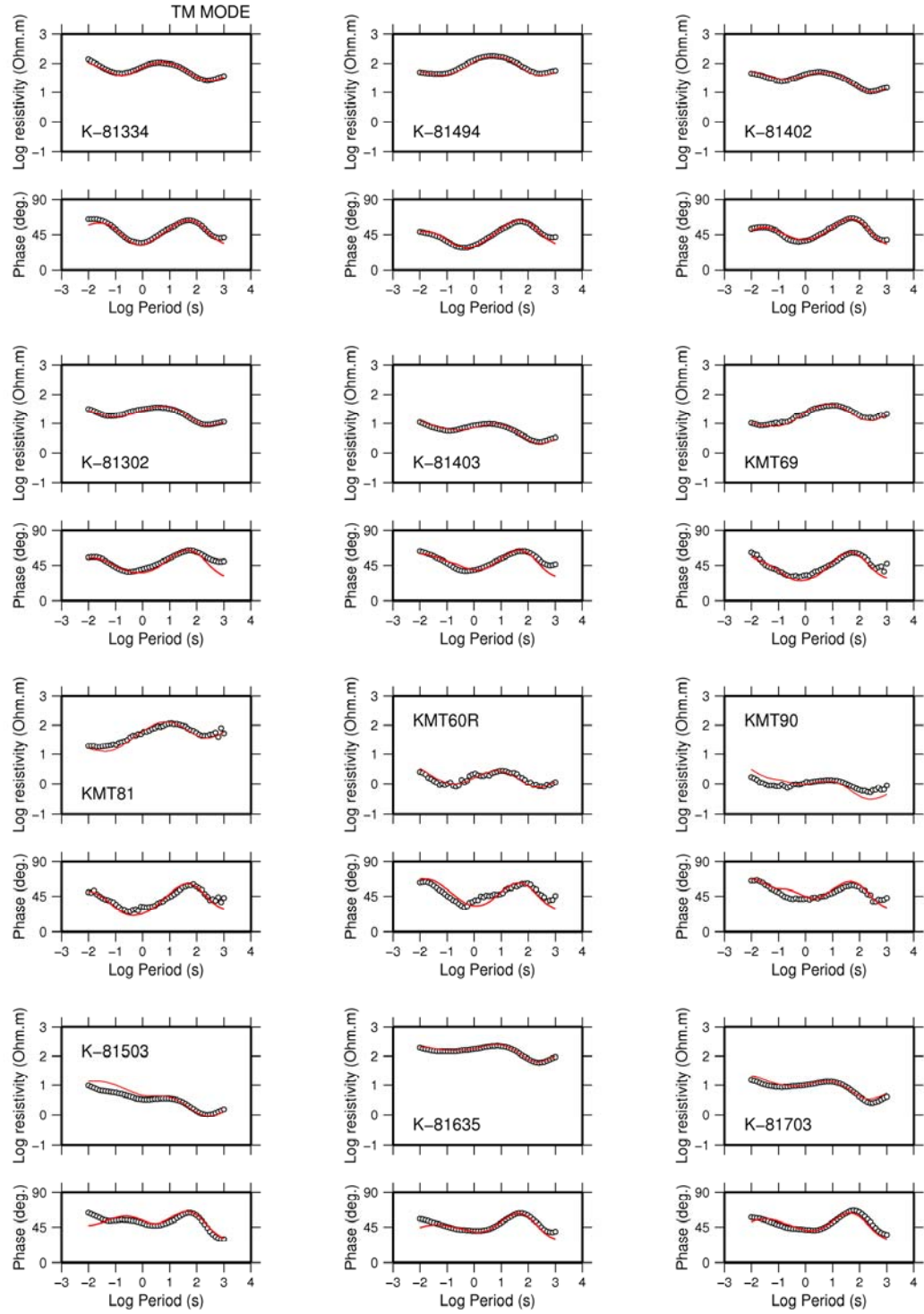
$$\nabla^2 \mathbf{E} = \nabla \times \frac{\partial \mathbf{B}}{\partial t} = \mu \frac{\partial}{\partial t} (\nabla \times \mathbf{H}) = \mu \sigma \frac{\partial \mathbf{E}}{\partial t} + \epsilon \mu \frac{\partial^2 \mathbf{E}}{\partial t^2} \quad (3.2a)$$

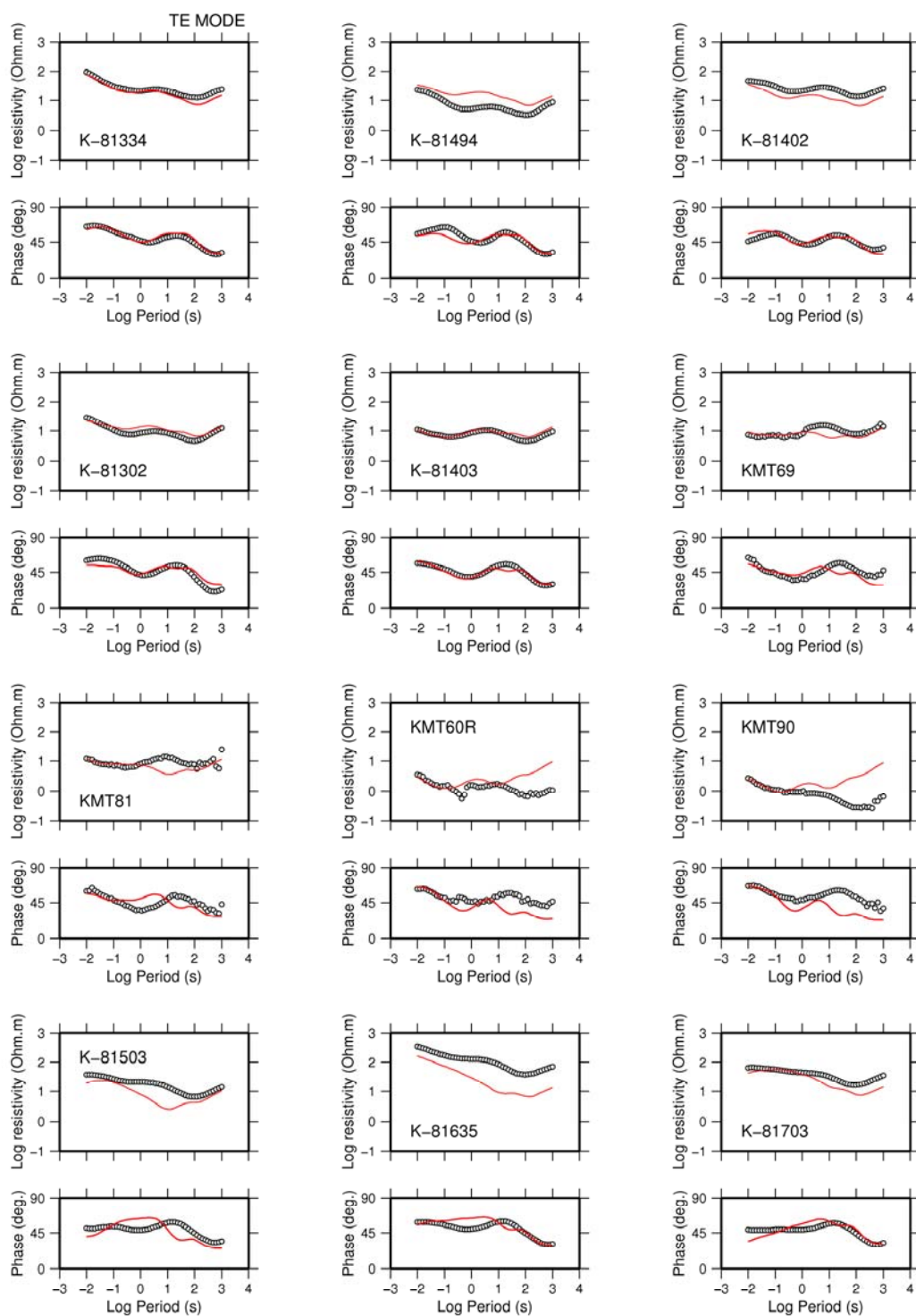
Similarly, by taking the curl of equation A2b, applying equation A1 and 3.1c (no free charges exist), we get:

$$\nabla^2 \mathbf{B} = -\sigma (\nabla \times \mathbf{E}) - \epsilon \frac{\partial}{\partial t} (\nabla \times \mathbf{E}) = \mu \sigma \frac{\partial \mathbf{B}}{\partial t} + \epsilon \mu \frac{\partial^2 \mathbf{B}}{\partial t^2} \quad (3.2b)$$

Appendix B: Observed data and calculated responses from TMTE join inversion

1. Profile AV7290





2. Profile AV7288

